Local Structure and Density of Liquid Fe-C-S Alloys at Moon's Core Conditions

Bin Zhao, Guillaume Morard, Eglantine Boulard, Silvia Boccato, Nicki Siersch, Attilio Rivoldini, Nicolas Guignot, Laura Henry, Andrew King, Claire Zurkowski, et al.

Local structure and density of liquid Fe-C-S alloys at Moon's core conditions

Bin Zhao[1], Guillaume Morard[2], Eglantine Boulard[1], Silvia Boccato[1], Nicki C. Siersch[1], Attilio Rivoldini[3], Nicolas Guignot[4], Laura Henry[4], Andrew King[4], Claire Zurkowski[5], Yingwei Fei[5], Daniele Antonangeli[1]

[1]Sorbonne Université, Muséum National d'Histoire Naturelle, UMR CNRS 7590, Institut de Minéralogie, de Physique des Matériaux et de Cosmochimie, IMPMC, 75005 Paris, France

[2]Université Grenoble Alpes, Université Savoie Mont Blanc, CNRS, IRD, Université Gustave Eiffel, ISTerre, 38000 Grenoble, France

[3]Royal Observatory of Belgium, Avenue Circulaire 3, B-1180 Brussels, Belgium

[4]Synchrotron SOLEIL, L'Orme de Merisiers, Saint Aubin-BP48, 91192 Gif-sur-Yvette, France

[5]Earth and Planets Laboratory, Carnegie Institution for Science, 5251 Broad Branch Road, N.W., Washington, DC 20015, USA

Corresponding author: Bin Zhao (bin.zhao@upmc.fr)

Key points:

We measured the local structure and density of liquid Fe-C-S alloys in the range of 1-5 GPa and 1600-1900 K.

A thermodynamic model based on asymmetric Margules formalism was built based on this data set.

We used this thermodynamic model to address three of the latest models of the Moon's core and to discuss the possible C and S content.

Abstract

The local structure and density of ternary Fe-C-S liquid alloys have been studied using a combination of in situ X-ray diffraction and absorption experiments between 1 and 5 GPa and 1600–1900 K. The addition of up to 12 at% of carbon (C) to Fe-S liquid alloys does not significantly modify the structure, which is largely controlled by the perturbation to the Fe-Fe network induced by S atoms. The liquid density determined from diffraction and/or absorption techniques allows us to build a non-ideal ternary mixing model as a function of pressure, temperature, and composition in terms of the content of alloying light elements. The composition of the Moon's core is addressed based on this thermodynamic model. Under the assumption of a homogeneous liquid core proposed by two recent Moon models, the sulfur content would be 27–36 wt% or 12–23 wt%, respectively, while the carbon content is mainly limited by the Fe-C-S miscibility gap, with an upper bound of 4.3 wt%. On the other hand, if the core is partially molten, the core temperature is necessarily lower than 1850 K estimated in the text, and the composition of both the inner and outer core would be controlled by aspects of the Fe-C-S phase diagram not yet sufficiently constrained.

Plain Language summary

Several geodetic and geochemical studies addressed the properties of the Moon's core, but its density remains poorly constrained. Core density is directly related to its chemical composition, which is crucial for better understanding Moon's origin and evolution. With carbon and sulfur being considered as two plausible light elements alloyed to iron to form the core, we selected a series of Fe-C-S compositions and studied the local structure and density of the corresponding liquids. The measured densities were integrated to build a thermodynamic model. Our results show that sulfur and carbon have a co-effect on the density and sound velocity of the liquid alloys, with sulfur playing a much more significant role. Consequently, the sulfur content is relatively well constrained for a given density, which however largely differs from model to model. On the contrary, the constraints on C content remain loose because of the smaller effect of C on the density and the inadequate knowledge of the Fe-C-S ternary phase diagram. While specific C and S ranges can be pointed out under the hypothesis of a fully molten core, the compositional constraints on a partially molten core are limited by the lack of knowledge of Fe-C-S phase diagram at pertinent conditions.

1.Introduction

Despite the large amount of seismic, geodetic, and electromagnetic data collected during the past half-century (e.g., Dickey et al., 1994; Hood et al., 1999; Konopliv et al., 1998), and the high accuracy measurements performed during the last 20 years, major questions remain open regarding the deepest regions of the Moon, especially its core (e.g., Lognonné et al., 2003; Nakamura et al., 1974; Toksöz et al., 1974). Electromagnetic sounding data from Lunar Prospector imply that the core region is metallic (Hood et al., 1999; Shimizu et al., 2013), while Apollo seismic data indicate high attenuation of acoustic waves passing through the core region (Nakamura, 2005; Weber et al., 2011). Other more specific but fundamental core properties such as size, density, and composition still remain rather uncertain (e.g., Garcia et al., 2011; Williams et al., 2014). To date, only a few consensuses have been reached: (a) The core should be at least partially molten in line with the moonquake records and geodetic observations (e.g., Lognonné & Johnson, 2007); (b) The mean core density is below that of pure iron, in order to match the measured moment of inertia (e.g., Garcia et al., 2019; Viswanathan et al., 2019); (c) Light elementsare needed in the core to decrease its crystallizing temperature and density (e.g., Garcia et al., 2019; Kuskov et al., 2021; Weber et al., 2011; Wieczorek et al., 2006), and sulfur is often favored as the main light element (e.g., Antonangeli et al., 2015; Jing et al., 2014; O'Neill, 1991; Weber et al., 2011). Based on joint inversion of available independent observations from Apollo missions, LLR (Lunar Laser Ranging) and GRAIL (Gravity Recovery and Interior Laboratory) data, and comparative geochemical analysis of Moon samples vs. bulk silicate Earth, several models have been put forward, which however show significant density spreading in the core, ranging from 4,200 to 7,000 kg/m3 (e.g., Garcia et al., 2011; Kuskov et al., 2021; Weber et al., 2011).

Sulfur is the most favored light element to be alloyed with iron in the Moon's core, because of its chemical affinity to iron at Moon's core conditions (siderophile behavior), and its effectiveness in decreasing the density of pure iron. In particular, considering the eutectic point of planetary-core-relevant iron alloys, the relatively low temperature of the Moon's interior (T between 1300 and 1900 K, e.g., Karato, 2013; Khan et al., 2006; Pommier et al., 2022; Wieczorek et al., 2006) points to an Fe- and S-rich core as the simplest explanation. Furthermore, the depletion of the lunar mantle in siderophile elements is possibly related to the presence of sulfur in the core (Rai & van Westrenen, 2014). Other light elements, such as oxygen and silicon, are not expected in significant concentrations as oxygen solubility into iron seems to be relatively low at the pressures pertinent to the Moon's core (Ricolleau et al., 2011), and the oxidizing conditions during the core differentiation do not favor silicon (Kilburn & Wood, 1997). On the other hand, carbon could be a potential light element component, with up to 4.8 wt% C estimated in the Moon's core lunar core, although its presence and abundance are debated (e.g., Steenstra et al., 2017 and references therein). As such, the phase diagram and the thermo-elastic properties of Fe-C and Fe-S binary

liquids have been intensively studied at pressures in the range of 1–10 GPa and temperatures between 1700 and 2200 K, forming the basis for discussing implications for Moon's core composition, origin, and thermal evolution.

Sulfur strongly decreases the melting temperature, density, and sound velocity of liquid iron (see Morard et al., 2018 and references therein) at Moon's core conditions. The phase diagram of Fe-S has been studied at pertinent P-T conditions by analysis of recovered samples and in situ X-ray diffraction (Fei et al., 1997, 2000). Sound velocity of liquid Fe-S has been studied by ultrasonic measurements (Jing et al., 2014; Nishida et al., 2016, 2020) and molecular dynamic calculations (Kuskov & Belashchenko, 2016). Density has been studied in situ by the sink/float method, X-ray diffraction, and absorption (Morard et al., 2018; Nishida et al., 2008, 2011; Sanloup et al., 2000; Xu et al., 2021). Thermodynamic models of liquid Fe-S at Moon's core conditions based on these experimental data show a strong non-ideal mixing behavior between liquid Fe and FeS (Morard et al., 2018; Terasaki et al., 2019; Xu et al., 2021). Macroscopic properties can be related to the local structure of the liquid, that is, how the Fe and S atoms are distributed in the short-range distance. In the binary liquid, sulfur is suggested to be incorporated interstitially in liquid iron (Shibazaki & Kono, 2018). Studies indicate that a small amount of sulfur does not significantly affect the local organization of the first coordination shells of the liquid, while the structure exhibits a progressively increased disorder for S concentration above 23.5 at% and the liquid becomes poorly organized for the end member FeS (Morard et al., 2018; Shibazaki & Kono, 2018).

Carbon is also an interstitial element in liquid iron (Shibazaki & Kono, 2018). However, as carbon atoms are much smaller in size compared to sulfur atoms, their inclusion perturbs the Fe liquid structure to a much lower extent. Unlike the disordered Fe-S alloys, Fe-C liquids at high pressure maintain a relatively well-defined local structure for C concentration up to 25 at% (Fe3C). Consequently, the density (Sanloup et al., 2011; Shimoyama et al., 2013; Terasaki et al., 2010) and sound velocity (Kuwabara et al., 2016; Shimoyama et al., 2016) of Fe-C liquids do not markedly decrease with increasing carbon content. A density discontinuity was first found in liquid Fe-5.7 wt% C around 6 GPa by Sanloup et al. (2011), and was attributed to a liquid-liquid phase transition of Fe-C at 5.2 GPa. This density discontinuity was reproduced on liquid Fe-3.5 wt% C (Shimoyama et al., 2013), and afterward, the phase transition was supported by the observation of a subtle structural change at ~5 GPa (Shibazaki et al., 2015).

While the two binary liquids have been well studied, the ternary Fe-C-S system, and in particular ternary Fe-C-S liquid alloys, remain far from being fully understood, with only a few data published on miscibility (Corgne et al., 2008; Dasgupta et al., 2009) and melting (Dasgupta et al., 2009; Deng et al., 2013). In this study, synchrotron X-ray diffraction and absorption experiments were conducted on ternary Fe-C-S liquid alloys in a Paris-Edinburgh cell up to 5 GPa and 1900 K to investigate in situ the

effect of the simultaneous incorporation of carbon and sulfur on the local structure and density of liquid iron alloys. The measured density data have been used to establish a thermodynamic model for Fe-C-S liquid solutions, which in turn can be used to help to determine the composition of the core of the Moon and other small planetary bodies.

2.Materials and Methods

2.1 Sample preparation

Iron (99.5%, Alfa Aesar), FeS (99.98%, Alfa Aesar), and graphite powders (99%, Alfa Aesar) were grounded in an agate mortar for 30 min to produce samples of nominal compositions of Fe-1.5 wt% C-4 wt% S (hereafter referred to as Fe-1.5C-4S), Fe-1.5C-8S, Fe-1.5C-15S, Fe-1.5C-22S, Fe-1.5C-30S, Fe-3C-4S, and Fe-3C-8S. Mixed powders were dried in a vacuum stove at 150°C for 1 hr, and loaded in BN capsules (Beamtime0720) or sapphire rings (Beamtime0921), prior to the X-ray diffraction and/or absorption experiments. While X-ray diffraction measurements have been conducted in both beamtimes, X-ray absorption measurements have been performed only in Beamtime0921, for which the sapphire capsules have been employed.

2.2 High-pressure in-situ X-ray diffraction experiments

In situ synchrotron X-ray diffraction and absorption experiments were carried out using the newly designed UToPEC (Ultrafast Tomography Paris Edinburgh Cell) (Boulard et al., 2018) at the PSICHÉ beamline, Synchrotron SOLEIL, France. The samples were loaded into a PEC assembly (shown in Figure S2 of Supporting Information S1) consisting of a sapphire ring, a BN capsule, a graphite furnace, and a boron epoxy gasket, similar to the one reported by Boulard et al. (2020). Pressure was generated by a pair of tungsten carbide anvils driven by a hydraulic pump, while high temperature generation was ensured by the above-mentioned graphite resistive furnace. Temperature as a function of power was calibrated in a dedicated run before the experiments by a non-destructive cross-calibration method (e.g., Parker et al., 2010) using the thermal Equation of State (EOS) of Pt, hBN, and MgO (Matsui et al., 2000, 2009; Y. Zhao et al., 1997) and the unit-cell volumes determined by X-ray diffraction at each power step. The error in temperature, including possible gradients, is estimated to be ±100 K. The hBN capsule, surrounding the sapphire ring, also served as the pressure calibrant (x-ray patterns collected on hBN close to sample are analyzed to derive volume, which in turn provide pressure by use of known thermal equation of state (Y. Zhao et al., 1997)). The high brilliance polychromatic X-ray beam with energy ranging from 10 to 90 keV was collimated to 25 × 50 μm2 (vertical × horizontal FWHM) by two slits before the sample. The diffracted beam was collected by a Ge solid-state detector.

In each experiment, the sample was initially cold compressed to the target pressure, and then molten by heating up at a rate of 100 K/min. At temperatures above 1150 K (corresponding to 300 W), the different phases present in the sample were checked every 50 W by diffraction. The fully molten status of the sample was pinpointed by the absence of sharp diffraction peaks of solids on top of the diffuse scattering signal from the liquid, and further confirmed by tomography. Indeed, thanks to the fast computed-tomography capabilities available at the PSICHÉ beamline (Boulard et al., 2018), the status of samples can be also monitored by 3D tomography images. Figure S3 shows the sequence obtained by increasing temperature from solid powder mixture to fully molten sample. We note that ternary alloy with high light element content at low pressure (< 3 GPa) proved to be immiscible, hence only high-pressure data were collected for the sulfur-rich samples. Once fully molten, a CAESAR (Combined Angle and Energy Dispersive Structure Analysis and Refinement) scan was collected by combining the recorded energy-dispersive diffraction pattern at angles from 2θ=2.5° to 29.5° with a step of 0.2° (King et al., 2022). The counting times for 2θ=2.5-10°, 10-20°, and 20-29.5° ranges were respectively 5 s, 10 s, and 20 s, for a total duration of the whole scan of about 20 minutes. The combined energy and 2θ ranges enable a data collection over an extended wave vector (Q), up to 20 $Å^{-1}$. A preset function controlled the motion of slits in front of the Ge detector and ensured signal collection from a fixed and constant volume of the sample irrespective of the angle.

The CAESAR data were analyzed on the basis of the methodology developed by Eggert et al. (2002) and Morard et al. (2014) implemented into the software AMORPHEUS (Boccato et al., 2022) to study the local structure and density of the liquids. In particular, the pair distribution function $g(r)$ and distribution function $F(r)$ (also referred to as reduced distribution function) are obtained from the collected $S(Q)$ by a Fourier transformation. For $r<r_{min}$ $F(r)= -4\pi r\rho$, where r_{min} is the minimum distance between two atoms due to the interatomic repulsive force, and ρ the atomic density. A figure of merit χ^2 as a function of r_{min} is defined to minimize the oscillation of $F(r)$ in the low r region. When χ^2 reaches the local minimum, the atomic density ρ is determined by the slope of $F(r)$ over $r<r_{min}$. The error on atomic density obtained by this method is empirically estimated by considering the effects on the resulting density due to the selected Q range, the self-absorption from the sample, and the scattering background residual from the surrounding materials and resulted in ±3 atoms/nm^3, in line with what previously reported in similar work (Morard et al., 2014). For materials of present interest, this yields an uncertainty on density about ±250 kg/m^3.

2.3. High-Pressure In Situ X-Ray Absorption Experiments

Predefined routines allow rapidly commuting the beamline setup from diffraction mode to absorption mode, while sharing the same general optics layout. Absorption profiles were thus collected right after each diffraction acquisition. In this configuration, the size of the incident beam was reduced to 10×10 μm^2 (vertical×horizontal FWHM) by collimating slits. An MgO polycrystalline sample was added into the optical path, between the sample and the detector, to act as a polychromator. On the downstream side, the detector was fixed at 8° with respect to the straight beam path, and the two diffraction peaks of MgO located at 37.5 keV (200) and 53.5 keV (220) were employed to record the absorption profile while scanning the sample (the intensities of the diffraction peaks are proportional to the beam intensity transmitted across the sample). Reference incident intensity was measured by translating the sample completely out of the beam. Detailed experimental procedure was described by Henry et al. (2022). One of the main advantages of this setup is that no extra optical paths or detectors were needed, and the absorption profile of the assembly was taken at the same experimental condition as the CAESAR scan.

Based on the Beer–Lambert law, it was possible to extract from the absorption profile the value of $(\mu\rho)_{P,T}$, the product of mass absorption coefficient and density at experimental P-T conditions. In order to disentangle the density from the absorption coefficient, we assumed the liquid to have the same absorption coefficient of the hot solid, which, in turn, is obtained from the absorption profile collected on the solid just before melting, imposing the density ρ_S inferred from energy-dispersive X-ray diffraction:

$$\rho_{P,T} = \frac{(\mu\rho)_{P,T}}{(\mu\rho)_S/\rho_S} \quad (1)$$

The details of data processing for diffraction and absorption can be found in the Supplementary Information S1.

3. Results

3.1 Liquid structure

Figure 1a shows the pair correlation function g(r) (or radial distribution function for isotropic media such as the liquids of the present study) together with partial g(r) from calculations available in the literature. Oscillations in the g(r)s become less pronounced for samples with 22.1 at% S or more, consistent with previous studies on Fe-S binary liquids (Morard et al., 2018; Shibazaki & Kono, 2018; Xu et al., 2021), in which the liquids were reported to show a more disordered structure for the S content of 23.5 at% S, 29.4 at% S, and 25.1 at% S, respectively. On the other hand, the inclusion of up to 18 at% of carbon in the ternary liquid seems not to have a detectable impact on the local structure as signatures of the second and third coordination shells are still distinguishable. The modification of the structure is controlled by the

interstitial inclusion of more massive S atoms that perturb the Fe-Fe network, while smaller C atoms can enter interstitial sites between Fe atoms without significant effect on the local structure. This is further supported by the variation in the atomic density shown in Figure S4 of Supporting Information S1. The atomic density with increasing S or C content shows opposite trends, highlighting the different effect of sulfur and carbon, while the atomic density of Fe-Si liquids does not significantly change with Si content, as Si atoms substitute iron atoms.

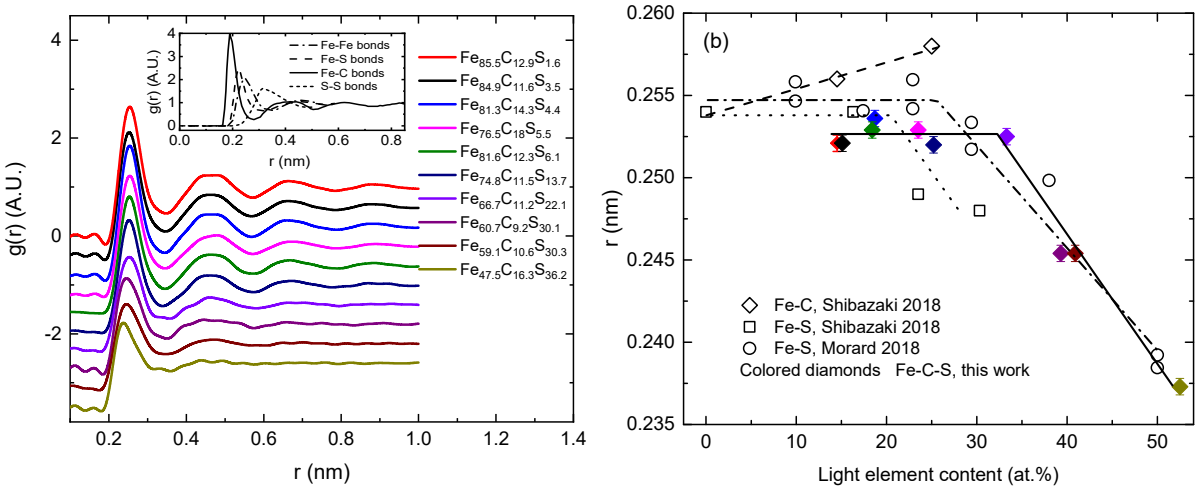

Figure 1 (a) Radial distribution function measured for Fe-C-S ternary liquids in the 1-5 GPa and 1700-1900 K range. Data are shown for increasing sulfur content (from the top to bottom). Inset: the partial $g(r)$ showing the individual contribution of Fe-Fe, Fe-S, and S-S bonds, calculated for a binary Fe-S liquid alloy with 23 at% S (Morard et al., 2018), and the partial $g(r)$ illustrating the Fe-C bonds calculated for a binary Fe-C alloy with 20 at% C (Lai et al., 2017). (b) First peak positions of the ternary alloys in comparison with results obtained for binary Fe-C and Fe-S at similar P-T condition (1.5-5.2 GPa and 1600-1980 K in Morard 2018, and 3-5 GPa, 1600-2000 K in Shibazaki 2018).

The most prominent feature in the $g(r)$ is the position (r_1) and intensity of the first peak corresponding to the first coordination sphere. r_1 as a function of total light element content is plotted in Figure1b and compared with results from literature obtained for binary liquids. Within the experimental uncertainties the r_1 value of Fe-S liquids is not observed to vary with S content for S addition up to ~20-25 at%, while it significantly decreases for higher concentration. As suggested by the calculated partial $g(r)$, this is likely due to the increased contribution of the shorter and covalent Fe-S bonds (Figure 1a). Since the scattering intensity is proportional to the square of the atomic number, the contribution from Fe-Fe and Fe-S bonds in the case of $Fe_{66.7}C_{11.2}S_{22.1}$ account, respectively, for ~65% and ~27% of the total signal (see Morard et al., 2008 and references there in), while the contribution from other bonds is negligible. Therefore, the formation of shorter Fe-S bonds moves the first peak position of the total $g(r)$ toward lower r value, while other bonds hardly have any visible effect. For binary Fe-C liquids, the addition of carbon

246 seems to move r_1 toward higher values according to available experimental data (Shibazaki and Kono,
247 2018), in apparent contrast with molecular dynamic calculations that indicate short Fe-C bonds (Lai et al.,
248 2017). This discrepancy may imply that the addition of carbon might have a more complex perturbation
249 effect other than simply forming the Fe-C bonds.

250 Our results of r_1 as a function of total light element content follow a trend qualitatively similar to that
251 reported for the binary Fe-S by Morard et al. (2018) and Shibazaki and Kono (2018), with a closer
252 agreement with values reported in the former. The r1 values of Fe-C-S liquids are not affected by the light
253 elements content in the alloy if below a critical amount of about 35 at%, above that value r_1 decreases
254 with increasing light element content. Up to 18 at% of C does not modify the two-regime behavior
255 observed for binary Fe-S liquid alloys nor the light element threshold defining the change in the regime.
256 Thus, in this context, C seems to play the same role as S in decreasing the r1 value, in agreement with the
257 length of the calculated Fe-C bonds (Lai et al., 2017), but in apparent contrast with the experimental r_1
258 value reported for the Fe-C liquids (Shibazaki and Kono, 2018).

259

260 3.2 Density

261 Table 1 summarizes the densities measured under the experimental conditions. Absorption measurements
262 were conducted only in the second of the two synchrotron beamtimes (*Beamtime0922*). Densities
263 obtained by diffraction and by absorption are consistent, with good agreement in the cases of S-rich
264 samples (e.g., measurements on $Fe_{60.7}C_{9.2}S_{30.1}$ and $Fe_{47.5}C_{16.3}S_{36.2}$), and the difference for measurements
265 even on $Fe_{74.8}C_{11.5}S_{13.7}$ is smaller than 8% between the two methods. When the two methods yield slightly
266 dissimilar results, densities measured by diffraction are systematically lower than those measured by
267 absorption. A possible reason is that collected diffraction signal is contributed from a sulfur-rich portion
268 of the sample. In fact, the diffraction method would be more sensitive to local inhomogeneity compared
269 to absorption if the diffracting volume is comparable in scale to the size of inhomogeneous regions (a few
270 tens of microns). On the other hand, as the absorption profile is taken on the whole sample, the error from
271 local inhomogeneity has been almost eliminated (i.e., the massive absorption coefficient is averaged).
272 Finally, and irrespective of the above consideration, we note that both values are used to calibrate
273 parameters of the thermodynamic model.

274

275 Table 1 Samples' composition, experimental P-T conditions, measured density and density rescaled to
276 1850 K, for both diffraction and absorption experiments.

Atomic proportion	Exp. T	Pressure	ρ by	ρ rescaled to	ρ by	ρ rescaled to

Fe	(%) C	S	(K)	(GPa)	diffraction (kg/m^3)[a]	1850K (kg/m^3)	absorption (kg/m^3)[b]	1850K (kg/m^3)
Beamtime0720								
84.9	11.6	3.5	1895	2.15	6780	6800(250)	/	/
85.5	12.9	1.6	1690	1.06	6900	6800(250)	/	/
81.3	14.3	4.4	1722	2.29	6740	6680(250)	/	/
			1895	2.09	6600	6620(250)	/	/
76.5	18.0	5.5	1625	2.52	6590	6490(250)	/	/
			1895	2.17	6430	6460(250)	/	/
Beamtime0921								
81.6	12.3	6.1	1760	3.86	6550	6510(250)	6830	6790(100)
			1850	3.70	6460	6460(250)	6460	6460(100)
74.8	11.5	13.7	1610	4.92	6200	6110(260)	6710	6610(110)
			1720	4.70	6180	6130(260)	6630	6570(110)
			1805	4.57	6110	6100(260)	6550	6530(110)
66.7	11.2	22.1	1760	3.72	/	/	5950	5920(110)
			1850	3.62	5620	5620(270)	6030	6030(110)
59.1	10.6	30.3	1760	3.44	5020	4990(280)	5220	5200(120)
			1850	3.31	5160	5160(280)	5200	5200(120)
60.7	9.2	30.1	1760	4.76	/	/	5590	5560(120)
			1850	4.35	5550	5550(280)	5510	5510(120)
47.5	16.3	36.2	1760	4.7	/	/	5140	5110(120)
			1850	4.42	4970	4970(280)	5060	5060(120)

[a] Uncertainty on density by XRD is ±250 kg/m^3 (see section 2.2)

[b] Uncertainty on density by absorption method is ±100 kg/m^3, considering the non-uniform effect of the environment and the fitting process (see supplementary Text S3).

3.3 Thermodynamic model

A thermodynamic solution model of the Fe-C-S liquid was built based on the thermal EOSs of the end members, Fe, FeS, and Fe_3C (parameters provided in Table S2 of Supporting Information S1) with their interactions modeled by an asymmetric Margules formulation (see Text S4 and Table S2 in Supporting Information S1; please refer to Tsuno et al. (2011) for more details on the formalism).

The fitted parameters to all the experimental data are listed in Table 2. Based on Equation S14 in Supporting Information S1, all relevant thermodynamic properties of Fe-C-S solutions can be computed from standard thermodynamic relations. The thermal expansion coefficients of each composition can be calculated according to its definition:

$$\alpha = \left(\frac{1}{V}\right)\left(\frac{\partial V}{\partial T}\right) \quad (2)$$

For comparison, the density measured at different temperature conditions are rescaled at the reference value of 1850 K by making use of the thermal expansion coefficients (Table 1), and the comparisons between ideal and non-ideal models are shown in Figure 2. The fitted Margules parameters for Fe and Fe3C are close to 0, indicating that Fe and Fe3C mix almost ideally at here-considered conditions. Comparing to the ideal mixing model in Figure 2a, the densities provided by Margules model in Figure 2b are in overall better agreement with the experimental data. Finally, we stress that although the here-established mixing model well accounts for the available experimental data and is suitable for density calculations for the Fe-C-S liquid system as a function of pressure and/or composition in the 0–5 GPa range, it may no longer be valid at higher pressure, since the density discontinuity of Fe-C liquid is due to a phase transition at 5.2 GPa (Sanloup et al., 2000).

Table 2 Fitted interaction Margules parameters

$W_{V,Fe-Fe_3C}$	0.2±0.2
W_{V,Fe_3C-Fe}	0±0.2
$W_{V,Fe-FeS}$	-2.2±0.4
$W_{V,FeS-Fe}$	-1.0±0.4
W_{V,Fe_3C-FeS}	-3.0±0.2
$W_{V,FeS-Fe_3C}$	0.8±0.2

Note. All the parameters are in cm^3/mol.

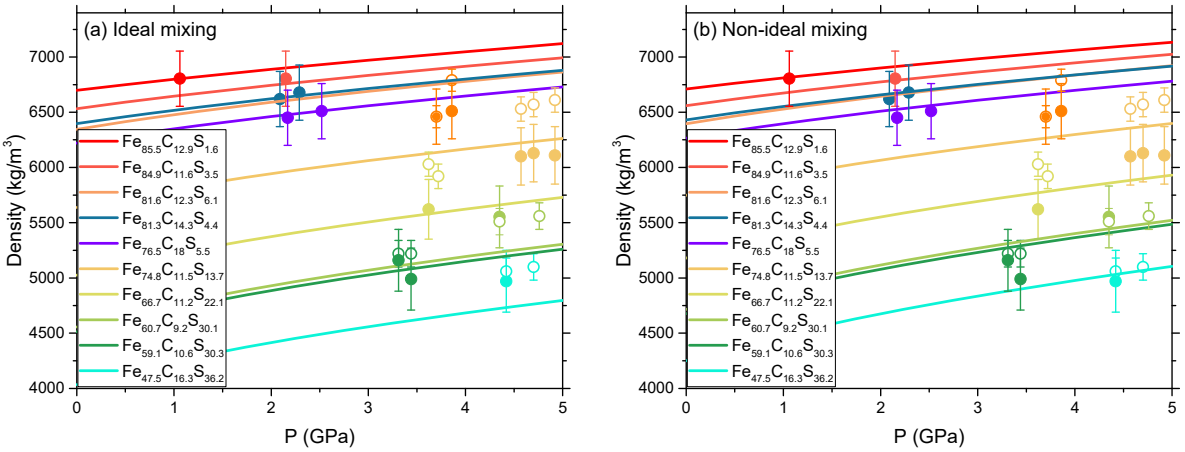

Figure 2 Density at 1850 K computed for selected compositions in the liquid Fe-C-S ternary system according to ideal (a) and non-ideal (b) thermodynamic models. (a) Ideal mixing model constructed based

306 on the properties of Fe, Fe_3C and FeS end members (Table S2 in Supporting Information S1). (b) Non-
307 ideal mixing model based on the Margules mixing rule. Open circles and filled circles are results from
308 absorption and diffraction measurements, respectively. The experimental uncertainties are mainly from
309 the limited Q range, self-absorption, and r_{min} fluctuation in the case of diffraction, and from minor sample
310 deformation and fitting procedure for absorption.

311

312 The density calculated for the liquid Fe-C-S ternary alloys at 5 GPa as a function of the light element
313 content is shown in Figure 3a and compared with data for binary Fe-S and Fe-C alloys from literature.
314 The uncertainties are from the fitting of the Margules parameters, which yielded ±35 – ±75 kg/m3 on the
315 density. The most recent studies on Fe-S liquid by diffraction (Morard et al., 2018) and absorption
316 (Terasaki et al., 2019) are in good agreement and provide higher density compared to earlier studies
317 (Sanloup et al., 2000), while results on Fe-C liquid by absorption are all within mutual uncertainties
318 (Sanloup et al., 2011; Shimoyama et al., 2013; Terasaki et al., 2010). The density of Fe-C-S alloy plots in
319 between those of binary alloys, indicating a co-effect of sulfur and carbon in decreasing the density of
320 pure iron. As alloys with high light element content reach the miscibility limit at low pressure (see
321 Dasgupta et al., 2009), the carbon content considered in this study is restricted to less than 18 at% to
322 model a homogeneous ternary liquid. The density is thus largely controlled by the sulfur content, with the
323 effect due to carbon inclusion minor as the direct consequence of the limited proportion of carbon in the
324 modeled alloys.

325 3.4 Sound velocity calculation

326 The compressional sound velocity of the ten compositions investigated in this study can be calculated at 5
327 GPa and 1850 K in an internally consistent way based on our thermodynamic model, following the
328 equation

$$v_p = \sqrt{\frac{K_T(1+\alpha\gamma T)}{\rho}} \quad (3)$$

329 where γ is the Grüneisen parameter, α the thermal expansion coefficient calculated by Eq. (2), ρ the
330 extrapolated density of the ternary alloy by the mixing model, and K_T the isothermal bulk modulus
331 calculated by its definition and the mixing model, Equation S14 in Supporting Information S1:

$$K_{1850K,P} = \left[-V\left(\frac{dP}{dV}\right)\right]_{1850K} \quad (4)$$

332 Since there is no experimentally determined γ for Fe-S, Fe-C, or Fe-C-S, the γ of ternary Fe-C-S samples
333 are calculated as:

$$\gamma = \frac{K_T V \alpha}{C_P - K_T V T \alpha^2} \quad (5)$$

where the C_P is the heat capacity at constant pressure of the ternary alloys, determined by the values of all the end members:

$$C_P = \frac{\partial(\sum_i x_i Q_i)}{\partial T} = \sum_i x_i C_{P,i} \quad (6)$$

where Q is the amount of heat and the subscript i represent each end members. The C_P of Fe, FeS, and Fe_3C are calculated with Equation 5 using the parameters provided in Table S2 of Supporting Information S1. The calculated thermo-elastic properties are provided in Table S3 of Supporting Information S1.

Here, we note that using other parameterizations of the bulk modulus of the alloys (e.g., Chen et al. 2014; Morard et al, 2018) and/or a value of γ=1.72 (e.g., Kuwabara et al., 2016; Shimoyama et al., 2016) fixed to that experimentally determined for liquid Fe (Anderson and Ahrens, 1994) lead to a ~15% higher compressibility, and consequently higher velocities, without modifying the reported trend.

Figure 3b shows the calculated sound velocity compared with the data from literature for the Fe-S and Fe-C binary systems. The errors are from the fitting of Margules parameters and the uncertainties of γ. The ternary data show some scatter but follow the trend defined for Fe-S alloys. We also note that the points showing higher values of sound velocity with respect to a linear trend are those with larger C fraction (e.g., the point at x=23.5, for which C content is 18 at%). While it is difficult to independently address the effect of S and C on velocities, the sound velocity of the liquid ternary alloy would offer a useful reference to model seismic velocities in the Moon's core.

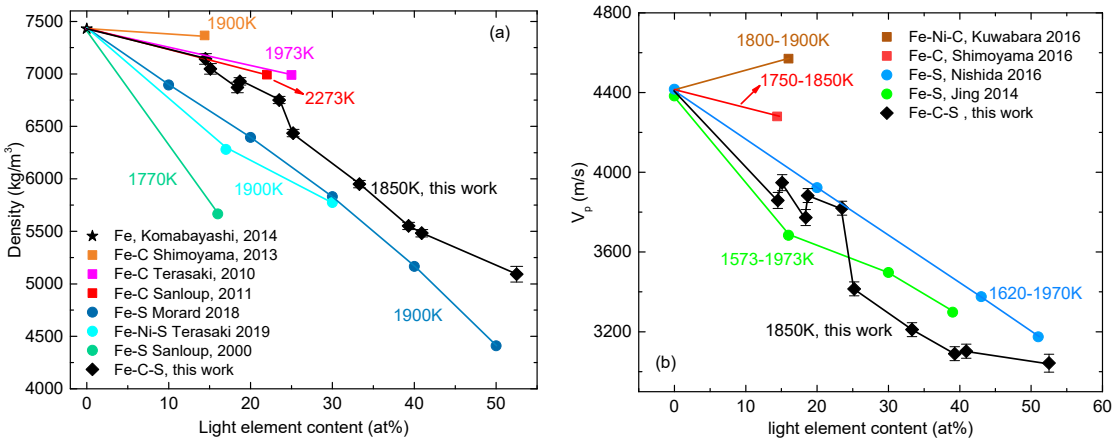

Figure 3 (a) Density and (b) sound velocity at 5 GPa modeled for the ternary Fe-C-S alloys as a function of light element content and compared with data for the binary Fe-S and Fe-C system. The reference

354 temperature for our model is 1850 K, while the temperature of other studies is annotated adjacent to the
355 data with the same color. Shown uncertainties on modeled properties account for uncertainties on used
356 thermo-elastic parameters and errors on fitting process. Lines across the points are guides for the eye.

357

358 ## 4 Discussion

359 The absence of data on the ternary Fe-C-S system so far has largely limited the discussion and the models
360 of the Moon's core to the binary Fe-S and Fe-C systems, or ternary system with Ni, which only
361 marginally affect the thermo-elastic properties of the alloy (e.g., Antonangeli et al., 2015; Jing et al., 2014;
362 Morard et al., 2018; Nishida et al., 2011; Terasaki et al., 2019). The current data set allows a step forward.
363 The local structure of ternary Fe-C-S liquid here experimentally determined for the first time show that
364 the shape of the $g(r)$ and in particular the position of the first coordination sphere evolves with increasing
365 light element content following the same trend of Fe-S liquids. As a first-order approximation, the limited
366 substitution of sulfur with carbon (~18 at%) doesn't affect the local structure of the ternary liquid.
367 However, the two elements have different quantitative effects on density and sound velocities (Figure 3).
368 Indeed, S lowers both density and sound velocity of liquid iron more significantly than C, as readily
369 visible from the experimental data of Fe-C and Fe-S liquids with the same atomic proportion.
370 Nevertheless, density and/or sound velocity constrained by seismological or geodetical observations can
371 be still used to address the carbon and sulfur content given this thermodynamic model if both are present
372 in the Moon's core.

373 Many Moon models were built by integrating various independent observables, including seismic,
374 electromagnetic, geodetic, and geochemical data. Great efforts have been made to interpret these
375 observables in terms of composition, but discrepancies still exist among studies, particularly concerning
376 the core (Garcia et al., 2019; Kuskov et al., 2021; Viswanathan et al., 2019 and references therein). To
377 discuss the possible content of sulfur and carbon in the Moon's core, two sets of density contours
378 assuming a hotter (1850 K) and cooler (1600 K) core are plotted in Figure 4, where densities proposed by
379 three of the latest Moon models (see Table 3 and associated references for more details) are correlated
380 with sulfur and carbon content based on here-presented results. In both cases, the Moon's core is assumed
381 to be at 5 GPa. Note that in Kuskov et al. (2021), the Moon's core is modeled with a solid inner core
382 surrounded by a liquid outer core, so that the solutions' space reported in Figure 4 corresponds to the C
383 and S content in the outer core, while being not detectable by the LLR or seismological data, the existence
384 of a solid inner core was deemed as uncertain by Garcia et al., (2019) and Viswanathan et al., (2019).
385 Therefore, a homogenous liquid core was assumed in their studies.

386

Table 3 Reference models of the Moon's core here considered for discussion.

	Garcia19	Viswanathan19	Kuskov21
Main data source	Seismic T_s, T_p Geodetic M, I/MR^2, k_2 Electromagnetic ρ_a	Geodetic Lunar Laser Ranging data, k_2; Crustal thickness and density	Seismic T_s, T_p Geodetic M, I/MR^2, k_2; Geochemical bulk concentration of FeO and Al_2O_3
Core status	At least a liquid outer core[a]	At least a liquid outer core[a]	Solid inner core + liquid outer core
Density of the (outer) core	4200 – 5200 kg/m^3	5560 – 6070 kg/m^3	6200 – 7000 kg/m^3

Note. Garcia19 is from model 2 in Garcia et al. (2019); Viswanathan19 is from Viswanathan et al. (2019), and Kuskov21 is from model E in Kuskov et al. (2021).

[a] The presence or not of an inner core is not constrained

Garcia et al., (2019) included two Moon's models with the core density lower than in Viswanathan et al. (2019) (hereafter Viswanathan19), resulting in a core prominently richer in sulfur. As the two models in Garcia et al. (2019) proposed quite similar core densities, the model 2 in that paper, hereafter Garcia19, using an updated geodetic data set, is taken for discussion here. As Fe, FeS, and Fe_3C were employed as end-members for the thermodynamic model, the mixing limit (i.e., the maximum light-element content) is defined by the curve linking FeS and Fe_3C in Figure 4. If this model were confirmed, the required sulfur content would range in 27 – 36 wt%, with the 250 K difference leading to a ~1 wt% shift in sulfur content, while the carbon content would be constrained by the ternary liquidus as a function of C and S content.

In the model Viswanathan19, the core oblateness as a function of radius was derived from two models, one with LLR-fitted polar MOI, and the other with a hydrostatic core model. The overlapped region indicates the core properties compatible with both models, which yield a core radius in the range of 381±12 km with a density of 5560 – 6070 kg/m^3. The proposed density and the corresponding C and S contents are shown in Figure 4. For a hotter core at 1850 K, carbon content spans from 0 to 4.6 wt%, approaching the miscibility gap (as our thermodynamic model is for a homogeneous liquid, the carbon content is not supposed to exceed this limit), and correspondingly, the sulfur content is constrained within 12 – 23 wt%. A colder core by 250 K would shift the contour to the S-richer side by ~1 wt% to balance the temperature effect.

The model Kuskov21 assumes a partially molten core of radius in the range 300-350 km. The favored densities of the liquid outer core and solid inner core are in the range of 6200-7000 kg/m^3 and 7500–7700 kg/m^3, respectively. The pseudobinary Fe(Ni)-S was considered in this paper, with a solid inner core

412 composed of iron (plus nickel and light elements at trace level) and an outer liquid core made of Fe-S. We
413 can then reconsider this model in the light of our results on the ternary Fe-C-S. Both, Fe and Fe_3C are
414 denser than the Fe-C-S liquids from which they crystallize and would be suitable candidates for an inner
415 core, with the actual crystallizing phase controlled by the bulk concentration of carbon in the liquid.

416 1. For a bulk composition on C-poor side (e.g., the Fe-0.33 wt% C-11.86 wt% S in Deng et al. (2013)), Fe
417 would be the first crystallizing solid phase, leaving a Fe-C-S liquid outer core. Whether an Fe inner core
418 would grow from the center (bottom-up), or Fe formed at the top of the core would snow across the liquid
419 core (top-down) depends on total light element content, in particular the S content (Xu et al., 2021).

420 2. For a bulk composition with intermediate light element content (e.g., the Fe-5 wt% C-5 wt% S, see
421 Dasgupta et al., 2009), Fe_3C would be the first solid phase to crystallize to form a solid inner core, leaving
422 a Fe-C-S liquid outer core until the entire available C is consumed. As in case (1), S content is expected to
423 largely control the top-down versus bottom-up crystallization regime.

424 3. For a bulk composition on C-rich side (e.g., the Fe-4.35 wt% C-7.85 wt% S, see Deng et al., 2013),
425 graphite will first form during the core cooling process and float upward to the core-mantle boundary,
426 followed by the crystallization of Fe_3C during the continuous temperature decrease to form an inner core.
427 When applied to the model of Kuskov21, only the latter stage is considered. Case (3) can thus be brought
428 back to case to (2).

429 Measurements (Dasgupta et al., 2009; Deng et al., 2013) on the Fe-C-S ternary system have supported the
430 above-outlined three crystallization regimes, which are strongly dependent on the bulk C and S content.
431 We stress, however, that with a limited number of experiments conducted only with a few specific
432 compositions, the C threshold between the C-poor and C-rich side, that is, the eutectic point, and how it
433 modifies with sulfur content, remain poorly constrained.

434 A solid inner core of fcc-iron with the density of 7500-7700 kg/m^3 was proposed in the model of
435 Kuskov2021. In this case, further limits in the amounts of light elements, beside the above-mentioned
436 eutectic, are placed by the liquidus (the existence of an inner core in equilibrium with melt imposes
437 conditions below those at liquidus). Melting experiments in the Fe–S–C system indicate the liquidus
438 temperature to decrease significantly compared to that in the Fe–S binary system by adding a very small
439 amount of carbon into the Fe–S system (Deng et al., 2013). In absence of precise determination of the
440 phase diagram of the Fe-C-S system, the ternary composition at liquidi temperature of 1850 K (hot case)
441 and 1600 K (cold case) are estimated as linear interpolation between results for the Fe-C and Fe-S binary
442 systems and shown as shaded area in the Fe corner (Figure 4). The entire compositional space
443 corresponding to the density of the outer core proposed in Kuskov21 lies outside this corner for a core at

1850 K. In other words, a relatively hot core at 1850 K could hardly support a solid inner core. If a colder core at 1600 K is assumed, the C and S content at liquidus are expected to significantly increase, enabling an overlap between the solutions in the compositional space accounting for proposed outer core density and the existence of Fe inner core. In this case the liquid outer core would have a sulfur and carbon content ranging from 13 to 5 and from 0 to 2.3 wt%, respectively.

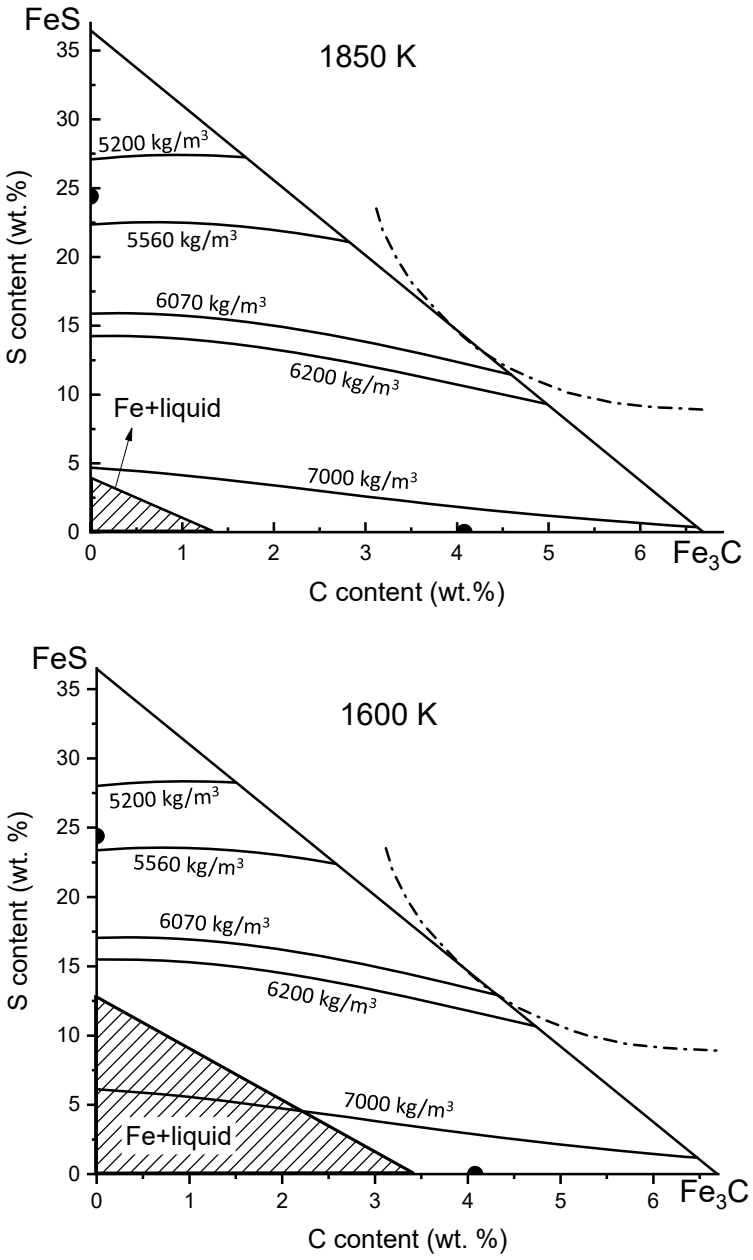

Figure 4 The carbon and sulfur content distribution within the liquid (outer) core assumed at 5 GPa and either 1850 K (top) or 1600 K (bottom) having density according to three recent Moon's models: Garcia19 (Garcia et al., 2019), Viswanathan19 (Viswanathan et al., 2019), and Kuskov21 (Kuskov et al., 2021). The shaded triangle shows the composition range for which the solid Fe phase (+C at solid solubility limit) is expected to be in coexistence with Fe-C-S liquid. The dotted-dash curve is the miscibility gap at 5 GPa and 1873 K for Fe-C-S liquid alloys by Dasgupta et al. (2009). The same miscibility gap was assumed for the lower temperature in the absence of applicable data. Eutectic compositions for the Fe-S (Buono & Walker, 2011) and Fe-C (Fei & Brosh, 2014) binary system at 5 GPa are also shown by the closed circles on the axes.

5 Conclusions

Liquid structures and densities of Fe-C-S alloys have been studied by a multi-techniques approach at high pressure and high temperature, up to 5 GPa and 1900 K, over a large range of carbon and sulfur content. The experimental data were employed to establish a non-ideal thermodynamic solution model for density and other thermo-elastic properties of liquid ternary alloys as a function of pressure and composition, which provides a useful database to discuss the composition of the core of small telluric planetary bodies.

Local structure, density and sound velocity of the ternary Fe-C-S liquids have been compared to those of binary Fe-C and Fe-S liquids. Although both interstitial, S and C affect the liquid structure differently, with $g(r)$ of ternary Fe-C-S liquid very close to the $g(r)$ of binary Fe-S liquid with the same light element content. At first approximation, the local structure of ternary liquids is thus controlled by the S content. Conversely, both density and sound velocity of ternary alloys show a co-effect of carbon and sulfur. With specific regards to density, values of ternary alloys are distributed between the upper and lower values provided, respectively, by Fe-C and Fe-S alloys having the same total amount of light elements. Still, the effect of S is more significant, lowering both density and sound velocities of the ternary Fe-C-S liquids with respect to pure Fe more significantly than C, as evident from the direct comparison of properties of ternary alloys with the same total amount of light elements but different C *vs*. S proportions.

Based on the acquired knowledge of the thermo-elastic properties of Fe-C-S alloys, and the derived thermodynamic model, we discussed the simultaneous presence of carbon and sulfur in the Moon's core. Three of the latest Moon's models have been considered, which propose different core states (fully molten vs. partially molten) and have quite different core densities, and thus light element content. Carbon, differently from sulfur, is hardly constrained on the sole basis of density and/or sound velocity. Assuming the Moon's core is composed of a homogeneous Fe-C-S liquid, the specific carbon and sulfur

content has been discussed on the basis of the two models assuming of a fully molten core (Viswanathan et al., 2019; Garcia et al., 2019) at two reference temperatures, 1850 K and 1600 K. Derived sulfur content in the 12 – 23 wt% range (Viswanathan et al., 2019) or 27 – 36 wt% for model 2 in Garcia et al. (2019), well above upper limits proposed on the basis of core differentiation models (e.g. Rai and van Westrenen, 2014). This apparent incompatibility between a light, S-rich core advocated by geophysical observations and an S-poor core put forward by core-differentiation models, metal-silicate partitioning and elemental abundances in the bulk silicate Moon, remains to be addressed. On the other hand, if the core were not fully molten (e.g., model E in Kuskov et al., 2021), in the Fe-C-S system, a solid inner core would be made of Fe or Fe_3C depending on whether the bulk C content is on the C-poor or C-rich side of the eutectic. The currently limited knowledge of the phase diagram and melting properties of the ternary Fe-C-S system does not allow an entirely quantitative discussion. The existence of a solid inner core puts more constraints on core's temperature since it must be below the liquidus. If we assume a core temperature of about 1850 K, the amounts of S and C required to match the outer core density proposed in model E by Kuskov et al. (2021) make the existence of a solid inner core rather unlikely. As the liquidus temperature at the Fe-rich side decreases with increasing S or C content, a cooler core can accommodate more light elements in the liquid outer core while having an fcc-Fe solid inner core, in qualitative agreement with the model of Kuskov21. Assuming a temperature of 1600 K, the sulfur and carbon content in the liquid outer core, in coexistence with an fcc-Fe (+C at solubility limit) inner core, would be 5 – 13 wt% and 2.7 – 0 wt% (the higher C content correlates with the lower S). However, for a solid inner core composed of Fe_3C, the light element budget in the liquid outer core strongly depends on a detailed understanding of the phase diagram and partial melting properties of the ternary Fe-C-S system, for which further studies are needed.

CRediT authorship contribution statement

Bin Zhao: Conceptualization, Data curation, Formal analysis, Investigation, Visualization, Writing – original draft, review & editing

Guillaume Morard: Conceptualization, Methodology, Investigation, Supervision, Project administration, Writing – review & editing

Eglantine Boulard: Methodology, Investigation, Writing – review & editing

Silvia Boccato: Investigation, Software, Writing – review & editing

Nicki C. Siersch: Investigation, Writing – review & editing

Attilio Rivoldini: Methodology, Writing – review & editing

Nicolas Guignot: Investigation, Resources, Software

Andrew King: Resources, Software

Laura Henry: Resources, Software

Claire Zurkowski: Resources, Writing – review & editing

Yingwei Fei: Resources, Writing – review & editing

Daniele Antonangeli: Conceptualization, Methodology, Investigation, Supervision, Project administration, Writing – review & editing, Funding acquisition

Data availability statement

Raw experimental data, the Python and Matlab code for data analysis have been published in the Zenodo online repository (B. Zhao et al., 2022).

Acknowledgements

The authors wish to thank Imène Estève for her help with sample analysis by SEM, and Michel Fialin and Nicolas Rividi for their help during microprobe analysis. Yann Le Godec is acknowledged for fruitful discussions and his help for the definition and preparation of the PEC assembly. We also thank James Badro and Nicolas Wehr for preliminary tests in piston cylinder press, Anat Shahar for kindly delivering our samples to the Earth and Planets Laboratory, Washington DC, and Emma Bullock for technical assistance. This project has received funding from the European Research Council (ERC) under the European Union's Horizon 2020 research and innovation Programme (grant number 724690). YF acknowledges NASA's support (80NSSC20K0337). The Scanning Electron Microscope (SEM) facility at IMPMC is supported by Région Ile de France grant SESAME 2006 N◦I-07-593/R, INSU-CNRS, Institute de Physique (INP)–CNRS, University Pierre et Marie Curie–Paris 6, and by the French National Research Agency (ANR) grant ANR-07-BLAN-0124-01. The authors acknowledge synchrotron SOLEIL for the provision of beamtime under proposals 20191835 and 20210144.

References

Anderson, W.W., & Ahrens, T.J. (1994). An equation of state for liquid iron and implications for the Earth's core. *Journal of Geophysical Research: Solid Earth*, *99*(B3), 4273-4284. https://doi.org/ 10.1029/93JB03158

Antonangeli, D., Morard, G., Schmerr, N.C., Komabayashi, T., Krisch, M., Fiquet, G., et al. (2015). Toward a mineral physics reference model for the Moon's core. *Proceedings of the National Academy of Sciences*, *112*(13), 3916-3919. https://doi.org/10.1073/pnas.1417490112

Boccato, S., Garino, Y., Morard, G., Zhao, B., Xu, F., Sanloup, C., King, A., et al. (2022). Amorpheus: a Python-based software for the treatment of X-ray scattering data of amorphous and liquid systems. *High Pressure Research*, *42*(1), 69-93. https://doi.org/10.1080/08957959.2022.2032032

Boulard, E., King, A., Guignot, N., Deslandes, J.P., Le Godec, Y., Perrillat, J.P., et al. (2018). High-speed tomography under extreme conditions at the PSICHE beamline of the SOLEIL Synchrotron. *Journal of Synchrotron Radiation*, *25*(3), 818-825. https://doi.org/10.1107/ S1600577518004861

Boulard, E., Denoual, C., Dewaele, A., King, A., Le Godec, Y., & Guignot, N. (2020). Following the phase transitions of iron in 3D with X-ray tomography and diffraction under extreme conditions. *Acta Materialia*, *192*, 30-39. https://doi.org/10.1016/j.actamat.2020.04.030

Buono, A.S., & Walker, D. (2011). The Fe-rich liquidus in the Fe–FeS system from 1 bar to 10 GPa. *Geochimica et Cosmochimica Acta*, *75*(8), 2072-2087. https://doi.org/10.1016/j.gca.2011.01.030

Chantler, C.T., Olsen, K., Dragoset, R.A., Chang, J., Kishore, A.R., Kotochigova, S.A., and Zucker, D.S. (2005). Detailed Tabulation of Atomic Form Factors, Photoelectric Absorption and Scattering Cross Section, and Mass Attenuation Coefficients for Z = 1-92 from E = 1-10 eV to E = 0.4-1.0 MeV. *NIST, Physical Measurement Laboratory*. https://dx.doi.org/10.18434/T4HS32

Chen, J., Yu, T., Huang, S., Girard, J., & Liu, X. (2014). Compressibility of liquid FeS measured using X-ray radiograph imaging. *Physics of the Earth and Planetary Interiors*, *228*, 294-299. https://doi.org/10.1016/j.pepi.2013.12.012

Corgne, A., Wood, B.J., & Fei, Y. (2008). C-and S-rich molten alloy immiscibility and core formation of planetesimals. *Geochimica et Cosmochimica Acta*, *72*(9), 2409-2416. https://doi.org/10.1016/ j.gca.2008.03.001

Dasgupta, R., Buono, A., Whelan, G., & Walker, D. (2009). High-pressure melting relations in Fe–C–S systems: Implications for formation, evolution, and structure of metallic cores in planetary bodies. *Geochimica et Cosmochimica Acta*, *73*(21), 6678-6691. https://doi.org/10.1016/ j.gca.2009.08.001

Deng, L., Fei, Y., Liu, X., Gong, Z., & Shahar, A. (2013). Effect of carbon, sulfur and silicon on iron melting at high pressure: Implications for composition and evolution of the planetary terrestrial cores. *Geochimica et Cosmochimica Acta*, *114*, 220-233. https://doi.org/10.1016/j.gca.2013.01.023

Dickey, J.O., Bender, P.L., Faller, J.E., Newhall, X.X., Ricklefs, R.L., Ries, J.G., et al. (1994). Lunar laser ranging: a continuing legacy of the Apollo program. *Science*, *265*(5171), 482-490. https://doi.org/10.1126/science.265.5171.482

Eggert, J.H., Weck, G., Loubeyre, P., & Mezouar, M. (2002). Quantitative structure factor and density measurements of high-pressure fluids in diamond anvil cells by x-ray diffraction: Argon and water. *Physical Review B*, *65*(17), p.174105. https://doi.org/10.1103/PhysRevB.65.174105

Fei, Y., Bertka, C.M., & Finger, L.W. (1997). High-pressure iron-sulfur compound, Fe3S2, and melting relations in the Fe-FeS system. *Science*, *275*(5306), 1621-1623. https://doi.org/10.1126/ science.275.5306.1621

Fei, Y., Li, J., Bertka, C.M., & Prewitt, C.T. (2000). Structure type and bulk modulus of Fe3S, a new iron-sulfur compound. *American Mineralogist*, *85*(11-12), 1830-1833. https://doi.org/10.2138/am-2000-11-1229

Fei, Y., & Brosh, E. (2014). Experimental study and thermodynamic calculations of phase relations in the Fe–C system at high pressure. *Earth and Planetary Science Letters*, *408*, 155-162. https://doi.org/10.1016/j.epsl.2014.09.044

Garcia, R.F., Gagnepain-Beyneix, J., Chevrot, S & Lognonné, P. (2011). Very preliminary reference Moon model. *Physics of the Earth and Planetary Interiors*, *188*(1-2), 96-113. https://doi.org/10.1016/j.pepi.2011.06.015

Garcia, R.F., Khan, A., Drilleau, M., Margerin, L., Kawamura, T., Sun, D., et al. (2019). Lunar seismology: An update on interior structure models. *Space Science Reviews*, *215*(8), 1-47. https://doi.org/10.1007/s11214-019-0613-y

589 Henry, L., Guignot, N., King, A., Giovenco, E., Deslandes, J.P., & Itié, J.P. (2022). In situ characterization of liquids at
590 high pressure combining X-ray tomography, X-ray diffraction and X-ray absorption using the white beam station at
591 PSICHÉ. *Journal of synchrotron radiation*, *29*(3). https://doi.org/10.1107/S1600577522003411

592 Hood, L.L., Mitchell, D.L., Lin, R.P., Acuna, M.H., & Binder, A.B. (1999). Initial measurements of the lunar induced
593 magnetic dipole moment using Lunar Prospector magnetometer data. *Geophysical Research Letters*, *26*(15), 2327-
594 2330. https://doi.org/10.1029/1999GL900487

595 Hubbell, J. H. and Seltzer, S. M. (2004). Tables of X-Ray mass attenuation coefficients and mass energy-absorption
596 coefficients from 1 keV to 20 MeV for elements Z = 1 to 92 and 48 additional substances of dosimetric interest.
597 Radiation *Physics Division, PML, NIST*. https://dx.doi.org/10.18434/T4D01F

598 Jing, Z., Wang, Y., Kono, Y., Yu, T., Sakamaki, T., Park, C., et al. (2014). Sound velocity of Fe–S liquids at high
599 pressure: Implications for the Moon's molten outer core. *Earth and Planetary Science Letters*, *396*, 78-87.
600 https://doi.org/10.1016/j.epsl.2014.04.015

601 Kilburn, M.R., & Wood, B.J. (1997). Metal–silicate partitioning and the incompatibility of S and Si during core
602 formation. *Earth and Planetary Science Letters*, *152*(1-4), 139-148. https://doi.org/10.1016/S0012-821X(97)00125-8

603 King, A., Guignot, N., Henry, L., Morard, G., Clark, A., Le Godec, Y., et al. (2022). Combined angular and energy
604 dispersive diffraction: optimized data acquisition, normalization and reduction. *Journal of Applied*
605 *Crystallography*, *55*(2). https://doi.org/10.1107/S1600576722000322

606 Knibbe, J.S., Rivoldini, A., Luginbuhl, S.M., Namur, O., Charlier, B., Mezouar, M., et al. (2021). Mercury's Interior
607 Structure Constrained by Density and P‐Wave Velocity Measurements of Liquid Fe-Si-C Alloys. *Journal of*
608 *Geophysical Research: Planets*, *126*(1), p.e 2020JE006651. https://doi.org/10.1029/2020JE006651

609 Komabayashi, T. (2014). Thermodynamics of melting relations in the system Fe-FeO at high pressure: Implications
610 for oxygen in the Earth's core. *Journal of Geophysical Research: Solid Earth*, *119*(5), 4164-4177. https://doi.org/
611 10.1002/2014JB010980

612 Konopliv, A.S., Binder, A.B., Hood, L.L., Kucinskas, A.B., Sjogren, W.L., & Williams, J.G. (1998). Improved gravity
613 field of the Moon from Lunar Prospector. *Science*, *281*(5382), 1476-1480. https://doi.org/10.1126/
614 science.281.5382.1476

615 Kuskov, O.L., & Belashchenko, D.K. (2016). Thermodynamic properties of Fe-S alloys from molecular dynamics
616 modeling: Implications for the lunar fluid core. *Physics of the Earth and Planetary Interiors*, *258*, 43-50.
617 https://doi.org/10.1016/j.pepi.2016.07.006

618 Kuskov, O.L., Kronrod, E.V., Matsumoto, K., & Kronrod, V.A. (2021). Physical Properties and Internal Structure of the
619 Central Region of the Moon. *Geochemistry International*, *59*(11), 1018-1037. https://doi.org/10.1134/S001670
620 2921110069

621 Kuwabara, S., Terasaki, H., Nishida, K., Shimoyama, Y., Takubo, Y., Higo, Y., et al. (2016). Sound velocity and
622 elastic properties of Fe–Ni and Fe–Ni–C liquids at high pressure. *Physics and Chemistry of Minerals*, *43*(3), 229-236.
623 https://doi.org/10.1007/s00269-015-0789-y

624 Lai, X., Chen, B., Wang, J., Kono, Y., & Zhu, F. (2017). Polyamorphic transformations in Fe-Ni-C liquids: Implications
625 for chemical evolution of terrestrial planets. *Journal of Geophysical Research: Solid Earth*, *122*(12), 9745-9754.
626 https://doi.org/10.1002/2017JB014835

627 Lognonné, P., Gagnepain-Beyneix, J., & Chenet, H. (2003). A new seismic model of the Moon: implications for
628 structure, thermal evolution and formation of the Moon. *Earth and Planetary Science Letters*, *211*(1-2), 27-44.
629 https://doi.org/10.1016/S0012-821X(03)00172-9

630 Lognonné, P., & Johnson, C. (2007). Planetary seismology. *Treatise on Geophysics*, *10*, 69-122.

631 Matsui, M., Parker, S.C., & Leslie, M. (2000). The MD simulation of the equation of state of MgO: Application as a
632 pressure calibration standard at high temperature and high pressure. *American Mineralogist*, *85*(2), 312-316.
633 https://doi.org/10.2138/am-2000-2-308

634 Matsui, M., Ito, E., Katsura, T., Yamazaki, D., Yoshino, T., Yokoyama, A., et al. (2009). The temperature-pressure-
635 volume equation of state of platinum. *Journal of Applied Physics*, *105*(1), p.013505.
636 https://doi.org/10.1063/1.3054331

637 Morard, G., Sanloup, C., Guillot, B., Fiquet, G., Mezouar, M., Perrillat, J.P., et al. (2008). In situ structural
638 investigation of Fe-S-Si immiscible liquid system and evolution of Fe-S bond properties with pressure. *Journal of*
639 *Geophysical Research: Solid Earth*, *113*(B10). https://doi.org/10.1029/ 2008JB005663

640 Morard, G., Garbarino, G., Antonangeli, D., Andrault, D., Guignot, N., Siebert, J., et al. (2014). Density measurements
641 and structural properties of liquid and amorphous metals under high pressure. *High Pressure Research*, *34*(1), 9-21.
642 https://doi.org/10.1080/08957959.2013.860137

643 Morard, G., Bouchet, J., Rivoldini, A., Antonangeli, D., Roberge, M., Boulard, E., et al. (2018). Liquid properties in the
644 Fe-FeS system under moderate pressure: Tool box to model small planetary cores. *American Mineralogist: Journal of*
645 *Earth and Planetary Materials*, *103*(11), 1770-1779. https://doi.org/10.2138/am-2018-6405

646 Nakamura, Y., Latham, G., Lammlein, D., Ewing, M., Duennebier, F., & Dorman, J. (1974). Deep lunar interior
647 inferred from recent seismic data. *Geophysical Research Letters*, *1*(3), 137-140.
648 https://doi.org/10.1029/GL001i003p00137

649 Nakamura, Y. (2005). Farside deep moonquakes and deep interior of the Moon. *Journal of Geophysical Research:*
650 *Planets*, *110*(E1). https://doi.org/10.1029/2004JE002332

651 Nishida, K., Terasaki, H., Ohtani, E., & Suzuki, A. (2008). The effect of sulfur content on density of the liquid Fe–S at
652 high pressure. *Physics and Chemistry of Minerals*, *35*(7), 417-423. https://doi.org/10.1007/s00269-008-0236-4

653 Nishida, K., Ohtani, E., Urakawa, S., Suzuki, A., Sakamaki, T., Terasaki, H., et al. (2011). Density measurement of
654 liquid FeS at high pressures using synchrotron X-ray absorption. *American Mineralogist*, *96*(5-6), 864-868.
655 https://doi.org/10.2138/am.2011.3616

656 O'neill, H.S.C. (1991). The origin of the Moon and the early history of the Earth—A chemical model. Part 1: The Moon.
657 *Geochimica et Cosmochimica Acta*, *55*(4), 1135-1157. https://doi.org/10.1016/0016-7037(91)90168-5

658 Parker, M., Sanloup, C., Tronche, E.J., Perrillat, J.P., Mezouar, M., Rai, N., et al. (2010). Calibration of a diamond
659 capsule cell assembly for in situ determination of liquid properties in the Paris–Edinburgh press. *High Pressure*
660 *Research*, *30*(2), 332-341. https://doi.org/10.1080/ 08957959.2010.484283

661 Rai, N., & van Westrenen, W. (2014). Lunar core formation: new constraints from metal–silicate partitioning of
662 siderophile elements. *Earth and Planetary Science Letters*, *388*, 343-352. https://doi.org/10.1016/ j.epsl.2013.12.001

663 Ricolleau, A., Fei, Y., Corgne, A., Siebert, J., & Badro, J. (2011). Oxygen and silicon contents of Earth's core from
664 high pressure metal–silicate partitioning experiments. *Earth and Planetary Science Letters*, *310*(3-4), 409-421.
665 https://doi.org/10.1016/j.epsl.2011.08.004

666 Sanloup, C., Guyot, F., Gillet, P., Fiquet, G., Mezouar, M., & Martinez, I. (2000). Density measurements of liquid Fe-S
667 alloys at high-pressure. *Geophysical Research Letters*, *27*(6), 811-814. https://doi.org/10.1029/1999GL008431

668 Sanloup, C., Van Westrenen, W., Dasgupta, R., Maynard-Casely, H., & Perrillat, J.P. (2011). Compressibility change
669 in iron-rich melt and implications for core formation models. *Earth and Planetary Science Letters*, *306*(1-2), 118-122.
670 https://doi.org/10.1016/j.epsl.2011.03.039

671 Shibazaki, Y., Kono, Y., & Fei, Y. (2015). Microscopic structural change in a liquid Fe-C alloy of~ 5 GPa. *Geophysical*
672 *Research Letters*, *42*(13), 5236-5242. https://doi.org/10.1002/2015GL064271

673 Shibazaki, Y., & Kono, Y. (2018). Effect of silicon, carbon, and sulfur on structure of liquid iron and implications for
674 structure-property relations in liquid iron-light element alloys. *Journal of Geophysical Research: Solid Earth*, *123*(6),
675 4697-4706. https://doi.org/10.1029/2018JB015456

676 Shimizu, H., Matsushima, M., Takahashi, F., Shibuya, H., & Tsunakawa, H. (2013). Constraint on the lunar core size
677 from electromagnetic sounding based on magnetic field observations by an orbiting satellite. *Icarus*, *222*(1), 32-43.
678 https://doi.org/10.1016/j.icarus.2012.10.029

679 Shimoyama, Y., Terasaki, H., Ohtani, E., Urakawa, S., Takubo, Y., Nishida, K., et al. (2013). Density of Fe-3.5 wt% C
680 liquid at high pressure and temperature and the effect of carbon on the density of the molten iron. *Physics of the*
681 *Earth and Planetary Interiors*, *224*, 77-82. https://doi.org/10.1016/j.pepi.2013.08.003

682 Shimoyama, Y., Terasaki, H., Urakawa, S., Takubo, Y., Kuwabara, S., Kishimoto, S., et al. (2016). Thermoelastic
683 properties of liquid Fe-C revealed by sound velocity and density measurements at high pressure. *Journal of*
684 *Geophysical Research: Solid Earth*, *121*(11), 7984-7995. https://doi.org/10.1002/2016JB012968

685 Steenstra, E.S., Lin, Y., Rai, N., Jansen, M., & van Westrenen, W. (2017a). Carbon as the dominant light element in
686 the lunar core. *American Mineralogist*, *102*(1), 92-97. https://doi.org/10.2138/am-2017-5727

687 Steenstra, E.S., Lin, Y., Dankers, D., Rai, N., Berndt, J., Matveev, S., et al. (2017b). The lunar core can be a major
688 reservoir for volatile elements S, Se, Te and Sb. *Scientific reports*, *7*(1), 1-8. https://doi.org/10.1038/s41598-017-
689 15203-0

690 Terasaki, H., Nishida, K., Shibazaki, Y., Sakamaki, T., Suzuki, A., Ohtani, E., et al. (2010). Density measurement of
691 Fe3C liquid using X-ray absorption image up to 10 GPa and effect of light elements on compressibility of liquid iron.
692 *Journal of Geophysical Research: Solid Earth*, *115*(B6). https://doi.org/10.1029/2009JB006905

693 Terasaki, H., Rivoldini, A., Shimoyama, Y., Nishida, K., Urakawa, S., Maki, M., et al. (2019). Pressure and
694 composition effects on sound velocity and density of core-forming liquids: Implication to core compositions of
695 terrestrial planets. *Journal of Geophysical Research: Planets*, *124*(8), 2272-2293.
696 https://doi.org/10.1029/2019JE005936

697 Toksöz, M.N., Dainty, A.M., Solomon, S.C., & Anderson, K.R. (1974). Structure of the Moon. *Reviews of*
698 *geophysics*, *12*(4), 539-567. https://doi.org/10.1029/RG012i004p00539

699 Tsujino, N., Nishihara, Y., Nakajima, Y., Takahashi, E., Funakoshi, K.I., & Higo, Y. (2013). Equation of state of γ-Fe:
700 Reference density for planetary cores. *Earth and Planetary Science Letters*, *375*, 244-253. https://doi.org/10.1016/
701 j.epsl.2013.05.040

702 Tsuno, K., Frost, D.J., & Rubie, D.C. (2011). The effects of nickel and sulphur on the core–mantle partitioning of
703 oxygen in Earth and Mars. *Physics of the Earth and Planetary Interiors*, *185*(1-2), 1-12. https://doi.org/10.1016/
704 j.pepi.2010.11.009

705 Viswanathan, V., Rambaux, N., Fienga, A., Laskar, J., & Gastineau, M. (2019). Observational constraint on the radius
706 and oblateness of the lunar core-mantle boundary. *Geophysical Research Letters*, *46*(13), 7295-7303.
707 https://doi.org/10.1029/2019GL082677

708 Weber, R.C., Lin, P.Y., Garnero, E.J., Williams, Q., & Lognonné, P. (2011). Seismic detection of the lunar
709 core. *science*, *331*(6015), 309-312. https://doi.org/10.1126/science.1199375

710 Wieczorek, M.A., Jolliff, B.L., Khan, A., Pritchard, M.E., Weiss, B.P., Williams, J.G., et al. (2006). The constitution and
711 structure of the lunar interior. *Reviews in mineralogy and geochemistry*, *60*(1), 221-364. https://doi.org/10.2138/
712 rmg.2006.60.3

713 Williams, J.G., Konopliv, A.S., Boggs, D.H., Park, R.S., Yuan, D.N., Lemoine, F.G., et al. (2014). Lunar interior
714 properties from the GRAIL mission. *Journal of Geophysical Research: Planets*, *119*(7), 1546-1578.
715 https://doi.org/10.1002/2013JE004559

716 Xu, F., Morard, G., Guignot, N., Rivoldini, A., Manthilake, G., Chantel, J., et al. (2021). Thermal expansion of liquid
717 Fe-S alloy at high pressure. *Earth and Planetary Science Letters*, *563*, p.116884. https://doi.org
718 /10.1016/j.epsl.2021.116884

719 Zhao, B., Morard, G., Boulard E., Boccato S., Siersch, N., Rivoldini, A., et al. (2022). Local structure and density of
720 liquid Fe-C-S alloys at Moon's core conditions [Dataset]. *Zenodo*. http://doi.org/10.5281/zenodo.7030984

721 Zhao, Y., Von Dreele, R.B., Weidner, D.J., & Schiferl, D. (1997). P-V-T Data of hexagonal boron nitride h BN and
722 determination of pressure and temperature using thermoelastic equations of state of multiple phases. *International*
723 *Journal of High Pressure Research*, *15*(6), 369-386. https://doi.org/10.1080/08957959708240481
724

[Journal of Geophysical Research: Planets]

Supporting Information for

[Local structure and density of liquid Fe-C-S alloys at Moon's core conditions]

[Bin Zhao[1], Guillaume Morard[2], Eglantine Boulard[1], Silvia Boccato[1], Nicki C. Siersch[1], Attilio Rivoldini[3], Nicolas Guignot[4], Laura Henry[4], Andrew King[4], Claire Zurkowski[5], Yingwei Fei[5], Daniele Antonangeli[1]]

[[1]Sorbonne Université, Muséum National d'Histoire Naturelle, UMR CNRS 7590, Institut de Minéralogie, de Physique des Matériaux et de Cosmochimie, IMPMC, 75005 Paris, France

[2]Université Grenoble Alpes, Université Savoie Mont Blanc, CNRS, IRD, Université Gustave Eiffel, ISTerre, 38000 Grenoble, France

[3]Royal Observatory of Belgium, Avenue Circulaire 3, B-1180 Brussels, Belgium

[4]Synchrotron SOLEIL, L'Orme de Merisiers, Saint Aubin-BP48, 91192 Gif-sur-Yvette, France

[5]Earth and Planets Laboratory, Carnegie Institution for Science, 5251 Broad Branch Road, N.W., Washington, DC 20015, USA]

Contents of this file

Text S1 to S4

Figures S1 to S8

Tables S1 to S4

Introduction

Text S1 describes the SEM and EPMA analysis of the recovered samples.

Text S2 and Text S3 provide detailed descriptions about the methods and data analysis procedures of diffraction and absorption techniques, respectively.

Text S4 provides a full description of the thermodynamic model.

Text S1. Analysis on the recovered samples

Quenched samples were mounted into epoxy resin and polished for scanning electron microscopy (SEM) and electron microprobe analysis (EMPA). The microstructures were analyzed by a ZEISS-ULTRA55 scanning electron microscope at the Institut de Minéralogie, de Physique des Matériaux et de Cosmochimie, Sorbonne Université. The backscattered electron images (Figure S1) of the quenched samples show 2 or 3 phases homogeneously distributed within the whole samples, with the S-rich and S-depleted portions clearly distinguishable due to the strong contrast. Energy-dispersive spectroscopy (EDS) mapping indicated there is no significant contamination in the sample from the surrounding materials (BN and Al_2O_3). The composition of each sample was quantified at the Earth and Planets Laboratory, Carnegie Institution for Science, with a JEOL8530F electron microprobe operated with an accelerating voltage of 15 kV and beam current of 20 nA. Following an experimental protocol like that in Deng et al. (2013), a calibration curve for carbon measurements was established based on the C *Kα* intensity of Fe_3C and a series of C-bearing NIST steels: Fe-0.008C, Fe-0.016C, Fe-0.392C, Fe-0.57C, and Fe-0.584C. The composition of different phases in each sample were determined from analysis carried out exploiting a focused beam of few microns, while the bulk composition by analysis performed with a defocused beam of 20×20 μm^2. Both obtained results are provided in Table S1. The measured carbon contents are systematically higher than the starting composition, while the sulfur contents don't significantly differ from the nominal values. The excessive carbon is likely coming from the graphite furnace, as BN is soft and tend to crack at experimental P-T condition so that a small amount C may have diffused across the capsule. Concerning the sample that was not possible to recover (Fe-1.5C-4S-3), the original sulfur content is adopted for further analysis (4 wt%), while a higher carbon content (3 wt%) is assumed, consistently with the other samples. When converting the sample composition from weight percent to atomic percent for further discussion, the observed traces of oxygen (Table S1), likely coming from sample's oxidation subsequent to the *in-situ* experiments, are neglected.

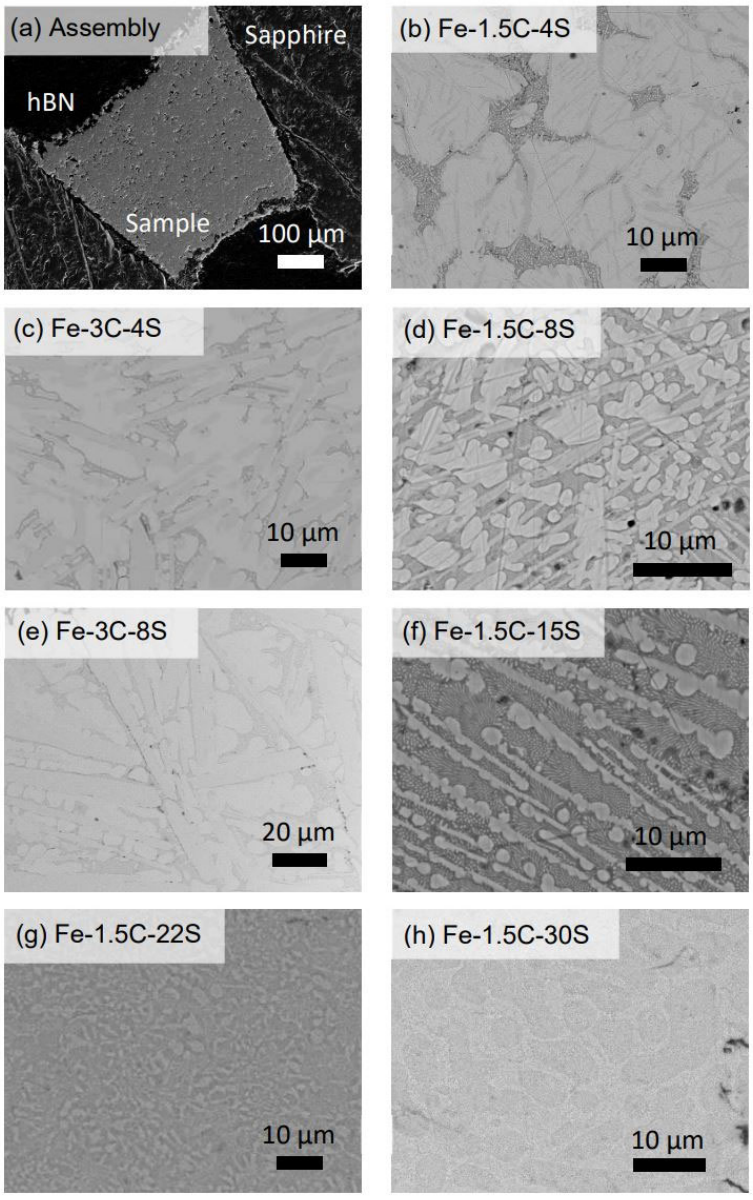

Figure S1 An example of a full view of a recovered assembly (a) and backscattered electron images of the different samples (b-h). Two phases are visible in the two most sulfur-rich samples (g and h) and three phases in the others (b-f). A lamellar-shaped carbon-rich phase with a composition close to Fe_3C can be observed for samples with sulfur content less than 15 wt% (b-f), which is similarly bright to the iron-rich phase (the bright phase with a round shape). With the increase of sulfur, the lamellar-shape C-rich and iron-

rich phases were replaced by a single carbon-bearing phase (g and h). The sulfur-rich phase corresponds to the dark regions present in all the samples.

Table S1. Quenched phases and bulk composition of each sample analyzed by EPMA.

Starting composition	Atomic proportion	Weight percent				Total	Notes
		Fe	C	S	O[d]		
Beamtime0720							
Fe-1.5C-4S-1	$Fe_{84.9}C_{11.6}S_{3.5}$	97.87(0.36)	1.43(0.52)	0.02(0.01)	0.08(0.02)	99.40(0.34)	Fe-rich phase
		93.1(0.98)	6.09 (0.65)	0.52 (0.67)	0.05(0.01)	99.77(0.26)	C-rich phase
		69.48(2.06)	1.23(0.53)	27.35(1.87)	0.25(0.05)	98.34(0.64)	S-rich phase
		95.88(3.62)	2.81(1.29)	2.28(3.21)	0.11(0.02)	101.08(0.83)	Bulk composition
Fe-1.5C-4S-2	$Fe_{85.5}C_{12.9}S_{1.6}$	97.82(0.83)	0.90(0.24)	0.03(0.01)	0.09(0.05)	98.83(0.65)	Fe-rich phase
		91.72(0.49)	6.08(0.31)	1.13(0.77)	0.09(0.05)	99.02(0.30)	C-rich phase
		67.58(2.73)	0.97(0.11)	29.24(2.48)	0.28(0.13)	98.07(0.45)	S-rich phase
		95.50(1.03)	3.11(0.46)	1.04(0.55)	0.53(0.10)	100.18(0.54)	Bulk composition
Fe-3C-4S	$Fe_{81.3}C_{14.3}S_{4.4}$	98.73(0.25)	1.11(0.13)	0.02(0.01)	0(0)	99.86(0.18)	Fe-rich phase
		93.53(0.21)	7.19(0.26)	0.02(0.01)	0(0)	100.74(0.17)	C-rich phase
		65.79(1.69)	1.03(0.14)	30.88(1.99)	0.10(0.03)	97.80(0.54)	S-rich phase
		94.06(2.44)	3.55(1.07)	2.98(2.10)	0.15(0.20)	100.75(0.55)	Bulk composition
Fe-3C-8S	$Fe_{76.5}C_{18}S_{5.5}$	97.13(0.19)	0.94(0.12)	0.03(0.01)	0(0)	98.11(0.22)	Fe-rich phase
		92.78(0.11)	6.60(0.19)	0.02(0.01)	0.01(0.01)	99.41(0.26)	C-rich phase
		67.58(4.05)	1.06(0.26)	30.11(4.00)	0.08(0.02)	98.85(0.33)	S-rich phase
		91.91(2.02)	4.64(1.29)	3.78(3.04)	0.48(0.14)	100.81(0.75)	Bulk composition
Beamtime0921							
Fe-1.5C-4S-3[a]	$Fe_{81.6}C_{12.3}S_{6.1}$	/	/	/	/	/	Recovery failure
Fe-1.5C-8S	$Fe_{74.8}C_{11.5}S_{13.7}$	96.66(0.44)	1.17(0.15)	0.34(0.30)	0.03(0.03)	98.20(0.14)	Fe-rich phase
		90.17(1.91)	6.22(1.02)	3.53(2.65)	0.12(0.09)	100.05(1.61)	C-rich phase
		75.96(1.14)	1.23(0.48)	21.09(1.24)	0.27(0.09)	98.55(0.89)	S-rich phase
		87.79(0.96)	2.89(0.28)	9.25(1.32)	0.06(0.06)	99.98(0.98)	Bulk composition
Fe-1.5C-15S[b]	$Fe_{66.7}C_{11}S_{22.1}$	86.29(3.21)	5.15(1.53)	7.96(3.43)	0.24(0.17)	99.65(1.73)	C-rich phase
		73.68(0.60)	1.41(0.28)	22.13(0.89)	0.64(0.35)	97.87(0.42)	S-rich phase
		80.77(0.5)	2.91(0.44)	15.40(0.70)	0(0)	99.09(0.31)	Bulk composition
Fe-1.5C-22S-1[c]	$Fe_{59.1}C_{10.6}S_{30.3}$	74.66(0.74)	2.88(0.64)	21.98(0.49)	0.13(0.02)	99.65(0.96)	Bulk composition
Fe-1.5C-22S-2[c]	$Fe_{60.7}C_{9.2}S_{30.1}$	75.49(0.41)	2.45(0.37)	21.55(0.22)	0.16(0.03)	99.65(0.44)	Bulk composition
Fe-1.5C-30S[c]	$Fe_{47.5}C_{16.3}S_{36.2}$	67.62(0.95)	4.97(0.25)	29.55(1.10)	0(0)	102.13(0.42)	Bulk composition

[a] Recovery was not able due to a blowout during the decompression.
[b] The Fe_3C phase visible in BSE image was not detected by microprobe due to the very small size of the grains, comparable to, when not smaller than the size of the focused beam.
[c] The texture of the two most S-rich sample is characterized by very small grains that do not allow distinguishing between C-rich and S-rich zones, therefore only the bulk composition is provided.
[d] The reported trace oxygen is thought from sample's oxidization occurred after the synchrotron experiments (July 2020 and September 2021) in the time lapse between SEM analysis (right after synchrotron experiments) and electron

microprobe analysis (April 2022) as the O amounts from two beamtimes are comparable if not slightly larger for *Beamtime0720*, indicating the use of sapphire rings in the second beamtime did not produce O contamination.

Text S2. Analysis of liquid X-ray scattering data

The analysis of the X-ray scattering data aims to determine the structural information of the liquid based on its relation with scattering signals. The density of the liquid can be subsequently extracted from the liquid structure.

The raw CAESAR data is a two-dimension intensity spectrum as a function of energy and 2θ. After a pre-normalization in terms of counting time, diffracted volume, the spectrum is shown in Figure S5. Because the beam source has lower brilliance at the two energy ends, the central portion of the energy range, with high signal-to-noise ratio (in 35-70 keV), was kept for further analysis. Normalizing the data with respect to spectrum of incident, the $I(E,2\theta)$ is rearranged in $I(Q)$ (Figure S6, left), with $Q = 4\pi E sin\theta/hc$ (where the E is the photon energy in J, h the Planck constant, and c the speed of light in vacuum). Details of the 2D CAESAR signal is presented in King et al., 2022.

The structure factor is calculated as follow (Example in Figure S6, middle):

$$S(Q) = \frac{I_{coh}(Q) - (\langle f^2 \rangle - \langle f \rangle^2)}{\langle f \rangle^2} = \frac{[\alpha I_{sample}(Q) - I_{incoh}(Q)] - (\langle f^2 \rangle - \langle f \rangle^2)}{\langle f \rangle^2} \quad \text{(S1)}$$

where the I_{coh} represents the intensity from coherent scattering, $I_{sample}(Q)$ the intensity measured from the sample, and $I_{incoh}(Q)$ the intensity from incoherent scattering. α is the normalization factor (Faber Ziman formalism), written as

$$\alpha = \frac{-2\pi\rho_0 + \int_0^{Qmax} (\sum I_{incoh}(Q) + \langle f^2 \rangle) Q^2 / \langle f \rangle^2 dQ}{\int_0^{Qmax} I_{sample}(Q) Q^2 / \langle f \rangle^2 dQ} \quad \text{(S2)}$$

In Eq. S1 and S2, f is the atomic form factor of the components. The atomic form factor of each element can be found in the NIST Standard Reference Database 66 (Chantler et al., 2005). $\langle f^2 \rangle = \sum x_n f_n^2(Q)$, and $\langle f \rangle^2 = \sum \sum x_n f_n(Q)\, x_m f_m(Q)$, where x_n is the proportion of nth element.

The distribution function $F(r)$ (example in Figure S6, right) and pair distribution function $g(r)$ are calculated by:

$$F(r) = \frac{2}{\pi} \int_0^{Q_{max}} Q(S(Q) - 1) \sin(Qr) dQ \equiv 4\pi r[\rho(r) - \rho_0] \quad \text{(S3)}$$

$$g(r) \equiv \frac{\rho(r)}{\rho_0} = 1 + \frac{F(r)}{4\pi r \rho_0} \quad \text{(S4)}$$

where $\rho(r)$ is the average atomic function and ρ_0 the average density. No atom exists within a threshold radius r_{min} to a certain atom because of the steric hindrance, so the $F(r)$ can be written as

$$F(r) = -4\pi r \rho_0 \ (r < r_{min}) \quad \text{(S5)}$$

In practice, since the limited Q value leads to an oscillation in the low-r region of $F(r)$ during the Fourier transform, an iteration procedure is needed to reduce the oscillation in the low-r region, and the $S(Q)$ at $i+1$th iteration is calculated by the inverse Fourier transform:

$$S_{i+1}(Q) = S_i(Q)\left[1 - \frac{1}{Q}\int_0^{r_{min}} \Delta F_i(r)\sin(Qr)\,dr\right] \quad \text{(S6)}$$

with the $\Delta F(r)$ in the first iteration using an estimated initial value ρ_0:

$$\Delta F_0(r) = -F_0(r) - 4\pi r\rho_0 \quad \text{(S7)}$$

The number of iterations is set to 5 to ensure the convergence (Eggert et al., 2002; Boccato et al., 2022). The final average atomic density is determined by minimizing a figure of merit:

$$\chi^2(r_{min}, Q_{max}, \rho_0) = \int_0^{r_{min}} [\Delta F(r)]^2 dr \quad \text{(S8)}$$

Figure S7 shows the minimization of χ^2 over a series of r_{min} and Q_{max}.

Text S3. Analysis of X-ray absorption data

The product $(\mu\rho)_{P,T}$ at experimental condition was determined by fitting the absorption profile to the Beer-Lambert law with the geometry of the sample (Nishida et al., 2011; Terasaki et al., 2010). The relationship of collected beam intensity and incident beam intensity follows a formula:

$$\frac{I}{I_0} = \exp(-\mu_s\rho_s t_s - \mu_c\rho_c t_c - \mu_e\rho_e t_e) \quad \text{(S9)}$$

where μ is mass absorption coefficient, ρ the density, and t the thickness, with the subscriptions of s, c, e representing sample, capsule, and environment. In practice, the contribution from environment was neglected, because all the gasket, furnace, and capsule are low-absorption materials, and the introduced non-uniform effects are weak (based on actual experimental geometry these can be assessed to lead to uncertainties on the density of less than 3%, accounted for the reported uncertainties of ±100 kg/m^3). Considering the geometry of the cylindrical capsule and sample, with the center noted by X_c, the intensity as a function of distance to the center would be written as

$$I = \begin{cases} I_0 \exp\left(-2\mu_c\rho_c\left(\sqrt{R-(x-X_c)^2} - \sqrt{r-(x-X_c)^2}\right) - 2\mu_s\rho_s\sqrt{r-(x-X_c)^2}\right) & x < r \\ I_0 \exp\left(-2\mu_c\rho_c\left(\sqrt{R-(x-X_c)^2}\right)\right) & r < x < R \\ I_0 & x > R \end{cases} \quad \text{(S10)}$$

where R and r are the radius of capsule and sample determined by the tomography at experimental condition, x is the distance to the sample center. The value of $\mu_c\rho_c$ and $\mu_s\rho_s$ can thus be determined by the fitting procedure. Figure S8 is an example of raw data compared with the fitted data. More details on the analysis can be found in Henry et al, 2022.

To extract the density of samples from the product $\mu_s\rho_s$, the μ_s was estimated by two means. One is following the formalism of the massive absorption coefficient of compounds:

$$\mu = \sum_i m_i\,\mu_i \quad \text{(S11)}$$

with the μ of each component taken from the NIST Standard Reference Database 126 (Hubbell, J.H. and Seltzer, S.M., 2004). The other is to calculate the μ from an absorption and diffraction scan before melting, which gives the product $\mu_s\rho_s$, and the density ρ_s of the solid sample, respectively. However, the densities from the two methods yield up to 8.6% discrepancy (Table S4). This large discrepancy originated from different μ determination may indicate the theoretical μ value is no longer appropriate in terms of the sample in the surrounding materials, since the absorption profile could include a component from the scattering of the gasket/capsule. Therefore, the μ from solid samples are employed in the analysis. Possible differences between nominal compositions and actual sample compositions, in particular concerning C content (see text S1), lead to variation in the estimated μ within reported uncertainties.

Text S4. The asymmetric Margules mixing model

In an asymmetric Margules formulation, the non-ideality of the Gibbs energy of the component *i* of a mixture is described by the addition of an excess contribution:

$$G_i = G_{i0} + G_{i,ex}(W) \tag{S12}$$

where G_i is the Gibbs energy of component i, G_{i0} the Gibbs energy at standard state, and $G_{i,ex}(W)$ the excessive Gibbs energy. W is the interactive Margules parameter which is assumed linear with pressure and temperature:

$$W(P,T) = W_0 + T \times W_S + P \times W_V \tag{S13}$$

Deriving the Gibbs energy with respect to pressure yields the volume. The volume of Fe-C-S liquids using Fe, FeS, and Fe_3C as end members is written as

$$V_{FeCS} = X_{Fe_3C}V_{Fe_3C} + X_{FeS}V_{FeS} + X_{Fe}V_{Fe} + X_{Fe_3C}V_{ex(\,Fe_3C)} + X_{FeS}V_{ex(\,FeS)} + X_{Fe}V_{ex(\,Fe)} \tag{S14}$$

The additional terms are excessive contributions to the volume, which are functions of the fraction of each component. For instance, the excessive volume contribution from Fe, *i.e.* $V_{ex(\,Fe)}$ is related to the other end members by:

$$\begin{aligned} V_{ex(\,Fe)} = {} & X_{FeS}^2[W_{V,Fe-FeS} + 2X_{Fe}\left(W_{V,FeS-Fe} - W_{V,Fe-FeS}\right)] \\ & + X_{Fe_3C}^2[W_{V,Fe-Fe_3C} + 2X_{Fe}\left(W_{V,Fe_3C-Fe} - W_{V,Fe-Fe_3C}\right)] \end{aligned} \tag{S15}$$

$$+2X_{Fe}X_{FeS}X_{Fe_3C}\left(W_{V,FeS-Fe}+W_{V,Fe_3C-Fe}\right)$$
$$-2X_{Fes}X_{Fe_3C}\left(X_{FeS}W_{V,Fe_3C-FeS}+X_{Fe_3C}W_{V,FeS-Fe_3C}\right)$$
$$+\frac{X_{Fe_3C}X_{FeS}(1-2X_{Fe})}{2}(W_{V,FeS-Fe}+W_{V,Fe-FeS}+W_{V,Fe_3C-Fe}$$
$$+W_{V,Fe-Fe_3C}+W_{V,Fe_3C-FeS}+W_{V,FeS-Fe_3C})$$

with the ternary interaction term neglected. $W_{V,i-J}$ is the volume interaction Margules parameter, which characterizes the interaction intensity of components i and j. We note that in this model the ternary interaction term is ignored. With the other two counterparts for FeS and Fe_3C, the mixed volumes given by Margules model are shown in Eq. (S16).

$$\begin{aligned}V_{Fe-C-S} = {} & X_{Fe_3C}V_{Fe_3C}+X_{FeS}V_{FeS}+X_{Fe}V_{Fe}+X_{Fe}X_{Fe_3C}^2W_{V,Fe-Fe_3C}+X_{Fe}X_{FeS}^2W_{V,Fe-FeS}\\ & +X_{Fe_3C}X_{Fe}^2W_{V,Fe_3C-Fe}+X_{Fe_3C}X_{FeS}^2W_{V,Fe_3C-FeS}\\ & +X_{Fes}X_{Fe}^2W_{V,FeS-Fe}+X_{Fes}X_{Fe_3C}^2W_{V,FeS-Fe_3C}\\ & +\frac{X_{Fe}X_{Fe_3C}X_{FeS}\left(3-2X_{Fe}-2X_{Fe_3C}-2X_{FeS}\right)}{2}(W_{V,Fe-Fe_3C}+W_{V,Fe-FeS}\\ & +W_{V,Fe_3C-Fe}+W_{V,Fe_3C-FeS}+W_{V,FeS-Fe}+W_{V,FeS-Fe_3C})\end{aligned} \tag{S16}$$

Thermo-elastic parameters defining the equation of state of liquid Fe, Fe_3C, and FeS are summarized in Table S2.

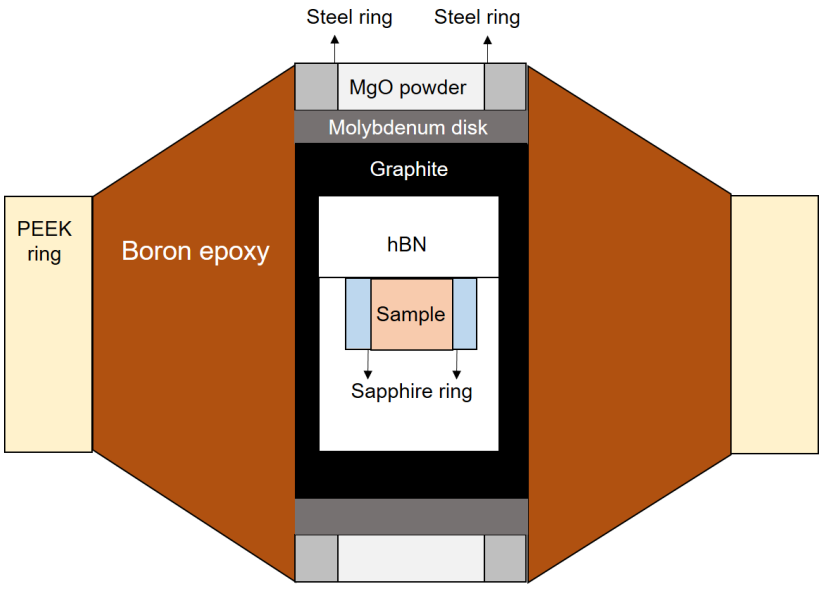

Figure S2 The internal parts of the 7-2.4 mm PE assembly used in the high pressure experiments.

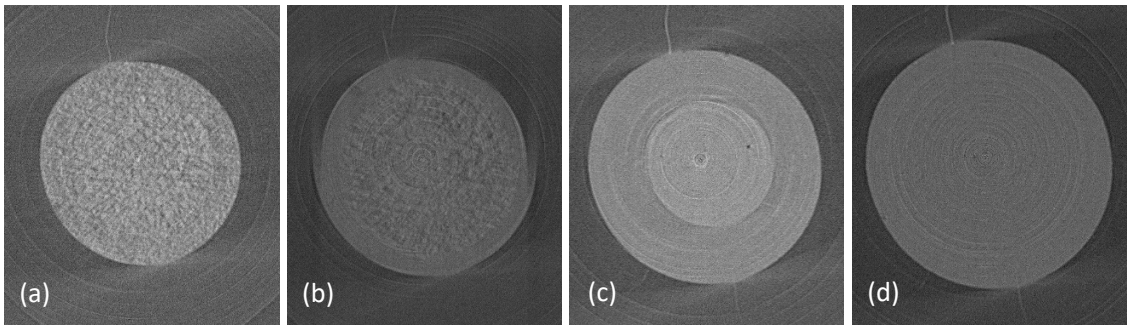

Figure S3 The melting of Fe-1.5C-8S observed by tomography. (a) Solid sample composed of Fe, FeS, and Fe_3C powders. (b) Onset of the melting. (c) Fully molten at a step of immiscible status including a C-rich part (light part in the center) + S-rich part (dark part). (d) The homogeneous liquid sample at the target temperature.

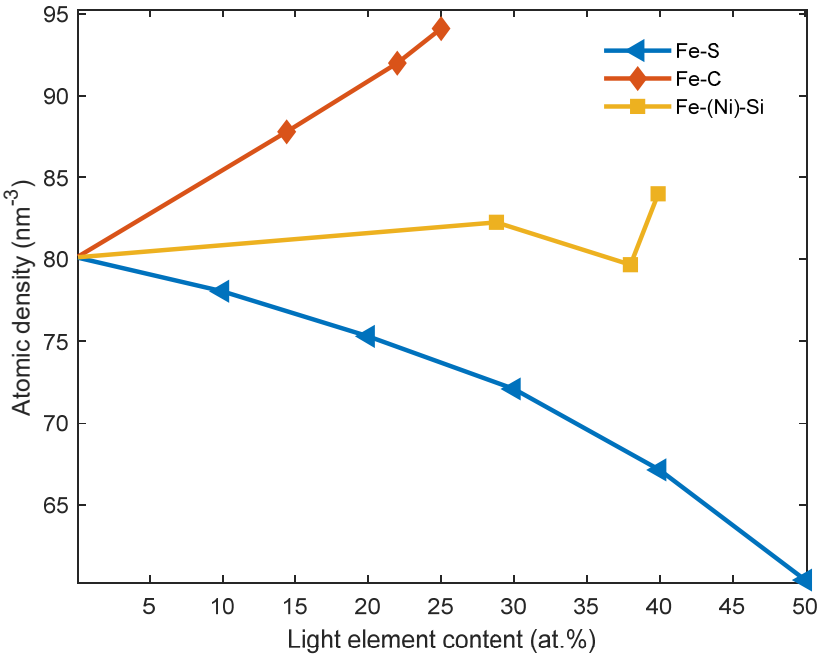

Figure S4 Atomic density of Fe-C, Fe-S, Fe(-Ni)-Si liquid calculated at 5 GPa from massive density following a formalism $\rho_{at} = \rho * N_A/M$, where ρ is the massive density, N_A the Avogadro number, and M the molar mass. The liquid Fe density is from Komabayashi 2014 at 1900K. Fe-C data are from Terasaki et al., 2010 ($Fe_{75}C_{25}$), Sanloup et al., 2011 ($Fe_{78}C_{22}$), and Shimoyama 2013 ($Fe_{86}C_{14}$) rescaled to the temperature of 1923K. Fe-S data are from Morard et al., 2018 at 1900K. Fe(-Ni)-Si data are from Sanloup et al., 2004 ($Fe_{71}Si_{29}$ and $Fe_{60}Si_{40}$) and Terasaki et al., 2019 ($Fe_{52}Ni_{10}Si_{38}$) at 1900K.

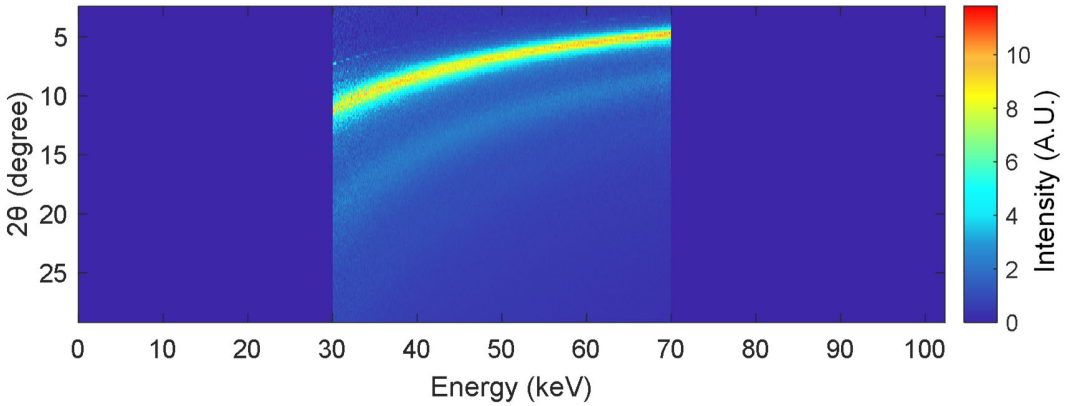

Figure S5 CAESAR data of the run Fe-1.5C-4S as a function of 2θ and energy after the normalization.

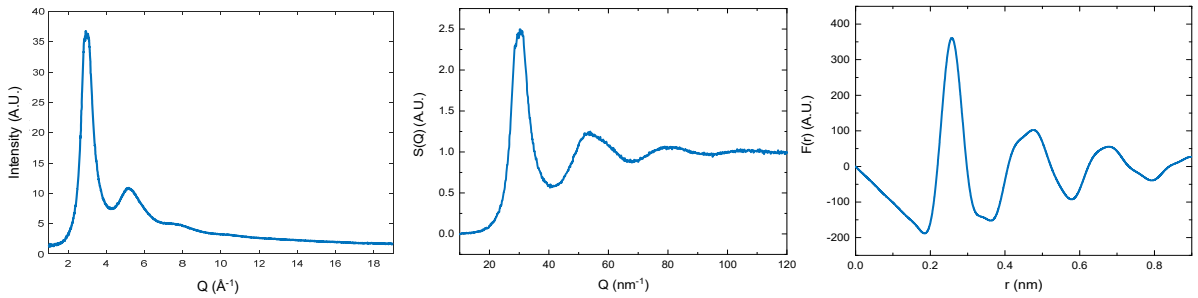

Figure S6 Left: Re-arranged Diffraction Intensity $I(Q)$ (left), Structure factor $S(Q)$ (middle), and distribution function $F(r)$ (right) of the run Fe-1.5C-4S.

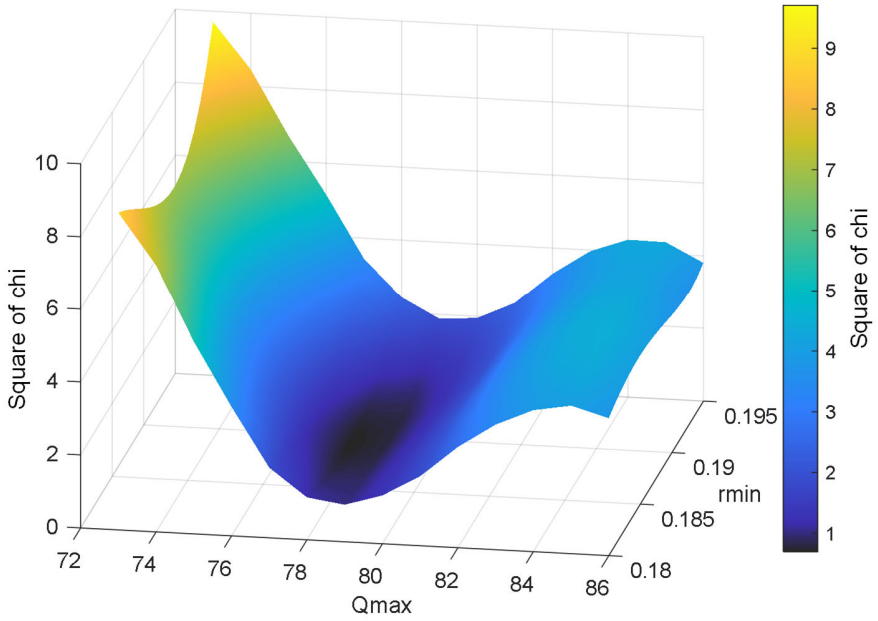

Figure S7 The loop for searching the minimum of χ^2 over a series of r_{min} for the sample Fe-1.5C-4S. The χ^2 reaches a local minimum when the r_{min} = 0.182 nm and Q_{max}=79, where the atomic density equals to 81.8, and the massive density 6780 kg/m^3.

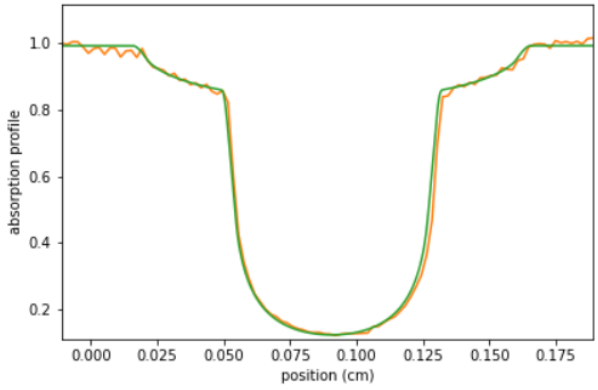

Figure S8. Raw absorption profile after normalization (orange) in comparison with fitted data (green) of $Fe_{74.8}C_{11.5}S_{13.7}$ at 4.92 GPa and 1610 K.

Table S2 Thermo-elastic parameters for Fe, Fe_3C, and FeS

Parameters	**Fe[a]**	**Fe_3C[b]**	**FeS[b]**
$V(P_0, T_0)$ (cm^3/mol)	6.88	26.68	22.96
K_{T0} (GPa)	148	75.66	17.02
K_T'	5.8	7.98	5.92
δ_T	5.1	9.43	5.92
$\alpha(P_0)$ ($10^{-5}K^{-1}$)	9	9.59	11.9
q	0.56	0.56	1.4
γ	1.73[c]	1.7	1.3
T_0(K)	298	1723	1650

a. Parameters from Komabayashi, 2014.
b. Parameters refitted by Knibbe et al., 2021.
c. Parameters from Anderson and Ahrens, 1994.
In all three cases the EOS is based on the Vinet formalism with the Anderson-Gruneisen model for the thermal components.

Table S3 Calculated thermo-elastic properties of all the samples at 1850 K and 5 GPa

Composition	K_T (GPa)	α ($\times 10^{-5}$ K^{-1})	C_P(J/K)	γ	v_p (m/s)
$Fe_{85.5}C_{12.9}S_{1.6}$	90.42	6.68	35.42	1.40	3859
$Fe_{84.9}C_{11.6}S_{3.5}$	92.74	6.67	35.25	1.47	3948
$Fe_{81.6}C_{12.3}S_{6.1}$	83.87	6.45	33.17	1.37	3773

$Fe_{81.3}C_{14.3}S_{4.4}$	89.12	6.39	32.71	1.43	3883
$Fe_{76.5}C_{18}S_{5.5}$	85.15	6.00	29.31	1.39	3820
$Fe_{74.8}C_{11.5}S_{13.7}$	66.41	6.08	29.21	1.15	3415
$Fe_{66.7}C_{11.2}S_{22.1}$	54.83	5.63	24.39	1.14	3211
$Fe_{60.7}C_{9.2}S_{30.1}$	47.89	5.34	21.07	1.08	3090
$Fe_{59.1}C_{10.6}S_{30.3}$	47.70	5.21	19.91	1.11	3103
$Fe_{47.5}C_{16.3}S_{36.2}$	42.21	4.54	12.14	1.39	3043

Table S4 Absorption data at experimental conditions

Beamtime0922

Composition	$\mu_s\rho_s$(cm^{-1})	T(K)	P(GPa)	μ calculated with NIST database @37.5 keV(cm^2/g)	ρ(kg/m^3)	μ from solid sample @ 37.5 keV (cm^2/g)	ρ(kg/m^3)
$Fe_{81.6}C_{12.3}S_{6.1}$	25.75	1760	3.86	4.02	6410	3.77	6830
	24.34	1850	3.70		6050		6460
$Fe_{74.8}C_{11.5}S_{13.7}$	26.00	1610	4.92	3.87	6720	3.88	6710
	25.69	1720	4.70		6640		6630
	25.39	1805	4.57		6560		6550
$Fe_{66.7}C_{11.2}S_{22.1}$	21.15	1760	3.72	3.69	5740	3.56	5950
	21.45	1850	3.62		5810		6030
$Fe_{59.1}C_{10.6}S_{30.3}$	17.38	1760	3.44	3.49	4980	3.32	5220
	17.32	1850	3.31		4960		5200
$Fe_{60.7}C_{9.2}S_{30.1}$	18.62	1760	4.76	3.52	5290	3.32	5590
	18.36	1850	4.35		5220		5510
$Fe_{47.5}C_{16.3}S_{36.2}$	15.01	1760	4.7	3.17	4730	2.92	5140
	14.78	1850	4.42		4660		5060

References:

Boccato, S., Garino, Y., Morard, G., Zhao, B., Xu, F., Sanloup, C., King, A., et al. (2022). Amorpheus: a Python-based software for the treatment of X-ray scattering data of amorphous and liquid systems. *High Pressure Research*, *42*(1), 69-93. https://doi.org/10.1080/08957959.2022.2032032

Eggert, J.H., Weck, G., Loubeyre, P., & Mezouar, M. (2002). Quantitative structure factor and density measurements of high-pressure fluids in diamond anvil cells by x-ray diffraction: Argon and water. *Physical Review B*, *65*(17), p.174105. https://doi.org/10.1103/PhysRevB.65.174105

Henry, L., Guignot, N., King, A., Giovenco, E., Deslandes, J.P., & Itié, J.P. (2022). In situ characterization of liquids at high pressure combining X-ray tomography, X-ray diffraction and X-ray absorption using the white beam station at PSICHÉ. *Journal of synchrotron radiation*, *29*(3). https://doi.org/10.1107/S1600577522003411

King, A., Guignot, N., Henry, L., Morard, G., Clark, A., Le Godec, Y., et al. (2022). Combined angular and energy dispersive diffraction: optimized data acquisition, normalization and reduction. *Journal of Applied Crystallography*, *55*(2). https://doi.org/10.1107/S1600576722000322

Hubbell, J. H. and Seltzer, S. M. (2004). Tables of X-Ray mass attenuation coefficients and mass energy-absorption coefficients from 1 keV to 20 MeV for elements Z = 1 to 92 and 48 additional substances of dosimetric interest. Radiation *Physics Division, PML, NIST*. https://dx.doi.org/10.18434/T4D01F

Chantler, C.T., Olsen, K., Dragoset, R.A., Chang, J., Kishore, A.R., Kotochigova, S.A., and Zucker, D.S. (2005). Detailed Tabulation of Atomic Form Factors, Photoelectric Absorption and Scattering Cross Section, and Mass Attenuation Coefficients for Z = 1-92 from E = 1-10 eV to E = 0.4-1.0 MeV. *NIST, Physical Measurement Laboratory.* https://dx.doi.org/10.18434/T4HS32